Development of a Reflective Polymer-Dispersed Liquid Crystal Shear Measurement System

Gina DeBenedictis

A thesis
submitted in partial fulfillment of the
requirements for the degree of

Master of Science in Aeronautics and Astronautics

University of Washington
2014

Committee:
Dana Dabiri, Chair
Gamal Khalil

Program Authorized to Offer Degree:
Aeronautics and Astronautics

University of Washington

Abstract

Development of a Polymer-Dispersed Liquid Crystal Shear Measurement System

Gina DeBenedictis
Chair of the Supervisory Committee:
Dana Dabiri
Department of Aeronautics and Astronautics

Polymer-dispersed liquid crystals as a shear force measurement system offer many advantages over conventional single-point measurement systems. They are non-intrusive while offering ideal 2-dimensional mapping of shear stresses across a surface. Furthermore, the inclusion of the liquid crystals within a polymer matrix allows for a reversible sensor that is self-adherent to testing surfaces. Previous testing has examined small-scale surface mapping and clear samples through which light may pass. This paper examines the expansion of polymer-dispersed liquid crystals to larger area mapping as well as reflective measurements, with measurements taken in multiple shear force configurations, confirming the validity of the reflective data.

Table of Contents

List of Figures

Acknowledgements

The author would first like to thank Professor Dana Dabiri and Professor Gamal Khalil for presenting the opportunity for this research project and for their continued support and assistance throughout the project. The author would further like to thank Professor Werner Kaminsky for his continued assistance with the project and the materials. Additional thanks are given to Dr. John West and Da-Wei Lee of Kent State University for their information and help. The author would also like to thank Wei-Hsin Tien for his guidance and daily support. The author wishes to extend a special thank you to Kenneth Low for his assistance near the end of the project. Finally, the author wishes to thank her family and friends for their understanding and support.

Chapter 1. Introduction

In the world of commercial aviation, the aerodynamic forces must be thoroughly understood, as they provide the basis for all design and analysis work. There are only two main forces that must be known: pressure, acting perpendicular to the body, and shear, acting parallel to the body. These forces combine to give the total lift and drag over an aircraft surface. The lift is crucial in defining the payload weight limitations, while drag determines the maximum thrust needed to accelerate the aircraft. The lift-to-drag ratio is used extensively in the initial mission profile weight sizing in aircraft design [1]. The aerodynamic efficiency is tied heavily to aircraft costs. A 7% increase in lift-to-drag ratio can lead to as much as 6% fuel savings, or 100,000 gallons of fuel per year [2].

Wind tunnel tests are used extensively to study and quantify these forces. Any sensor designed to measure a flow property must be chosen carefully based on several requirements. First, the sensor must not intrude into the flow, disrupting the flow and changing the value that is measured. Second, the sensor must allow for high resolution of spatial mapping. Point measurements can miss critical details. A robust sensor must be one that does not impose resolution limitations. Similarly, the sensor must have good temporal resolution to be able to respond to the smallest time scale changes in flow. Finally, the ideal sensor is relatively simple to use with repeatable results.

1.1. Shear Force Measurements

Shear force measurements present more difficulties than pressure measurements due to the limitations of single value methods. As mentioned previously, the sensor used must also be non-intrusive and give good 2-D mapping of the surface. While many shear sensors exist and are currently in use, not all of them match these strict requirements. Four current technologies will be presented: oil film interferometry, floating elements, MEMS, and liquid crystals. Of these four, the first three represent single point measurements, while the fourth is a true 2-D measurement system. Information regarding additional details of these shear stress measurements can be found in [3] and [4].

1.1.1. Oil Film Interferometry

Oil film interferometry (OFI) is one of many time-averaged methods for measuring shear stress. The relative simplicity of the calculations needed to derive the shear stress as well as the minimal equipment needed make this method highly appealing. OFI makes use of the known thin-oil-film-equation and the fact that oil films will thin with an applied shear force to a surface [3].

The use of oil films was first introduced as a qualitative means of visualizing streamlines along a body [5], [6]. The three forces impacting an oil film are gravity, pressure gradients, and skin friction. For a thin enough film, only skin friction determines the flow of the oil, with surface curvature being represented by the presence of gravitational forces [6].

The overall method is very simple. A schematic of the typical setup is shown in Figure 1. A droplet of oil placed on the surface of the body thins with the application of the shear force. The oil droplet itself is thin enough so that it doesn't interfere with the flow. Light from a monochromatic source shines onto the body. Some of the light is reflected off the surface of the oil droplet, while some of the light passes through the oil droplet and is reflected off the surface of the body [3].

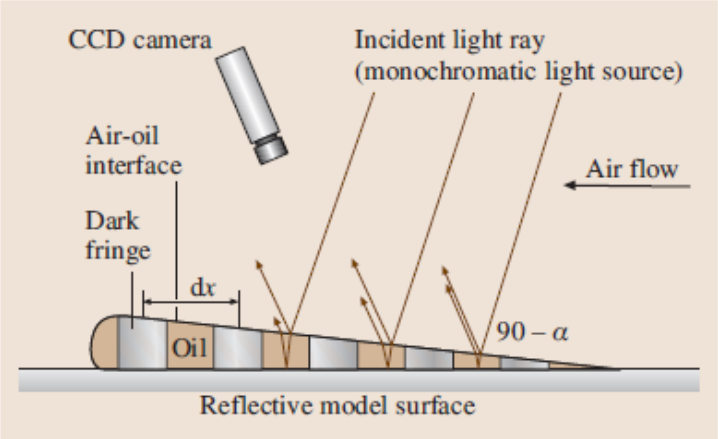

Figure 1: Setup for OFI shear stress measurement technique, obtained from [3], p. 876.

These light waves are captured with a CCD camera and appear as a fringe pattern consisting of dark and light bands due to the constructive and destructive interference of the

different waves. Figure 2 shows progressive time images with the application of a shear force. As the shear force is increased, the fringe pattern becomes more pronounced.

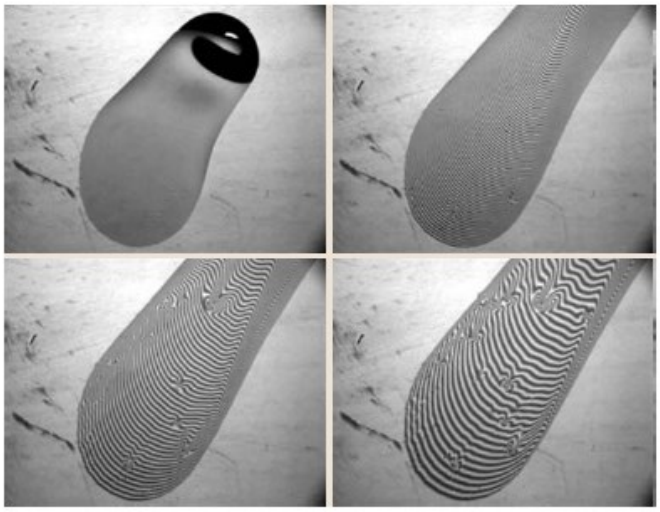

Figure 2: Interference fringe pattern seen in OFI measurements, obtained from [3], p. 877.

A simplified version of the thin-oil-film equation can be applied to determine the changing oil film thickness using the number of dark bands. This can then be used to find the time-averaged shear stress [3].

The oil has been shown to flow in the direction of the surface shear force except near separation, independent of oil viscosity. Furthermore, the oil film is thin enough to not impact the flow. However, a less viscous oil will have a greater impact on the boundary layer. In general, the method works best for low speed, incompressible, laminar flow [5].

While the calculations and equipment needed are quite simple, OFI presents several drawbacks. The biggest drawback of this sensor technique is the limited spatial resolution of this point measurement system. The individual droplets must be placed far enough away from one another so that it's impossible for them to run into each other. Additional consideration must be made when choosing the surface material and the oil to be used. Different surface materials produce better fringe patterns. The oil chosen should be temperature insensitive so as to limit the sources of error. The oil should also have a fairly low vapor pressure, as evaporation can cause the oil films to thin faster than they should. Other sources of error include the presence of dust and humidity in the testing environment [3].

Another large drawback of the OFI method is the low temporal resolution. The assumption that the effects of gravity and surface pressure gradients can be neglected is only valid for a long time-frame, as it is only for the case of very thin films that these forces can be neglected, with oil film thickness being inversely proportional to time [6]. Furthermore, the simplified version of the thin-oil-film equation is valid only for constant stress [3]. This limits the OFI measurement technique to steady-state flows only, where a lack of high temporal resolution is not as severe an issue.

1.1.2. Floating Element Sensors

Another class of shear sensors is the time-resolved methods, which includes floating element sensors. These sensors are small portions of the aerodynamic surface that are tethered to the surface in such a manner that allows them to still move, or "float." Either the force required to keep the floating element in place or the displacement of the floating element after an applied force can be measured to give the shear force. This requires that calibrations to a known force be performed beforehand, which can be done easily using a pulley-mass system [3].

One major benefit of the floating element method is that it directly measures the shear force, unlike some other time-resolved measurement systems. It also does not require any restrictions on the flow, and is therefore completely independent of flow properties. However, there are a number of drawbacks. As with the OFI method, the floating elements give point measurements, and the continuity of measurements is dictated by the locations of these sensors. Furthermore, the sampling frequency of the sensor must be sufficient to capture the time-varying conditions of the flow.

Additional issues arise from the size and placement of the elements. The size must be large enough to register a force, but small enough to measure local conditions. The element must be placed so as to be properly aligned and without gaps around the edges. Whether the element is protruding or recessed, small eddies can occur at the corners, generating additional lip forces that severely impact the sensor measurements. Figure 3 shows some of the common errors associated with misplacement of the elements [3].

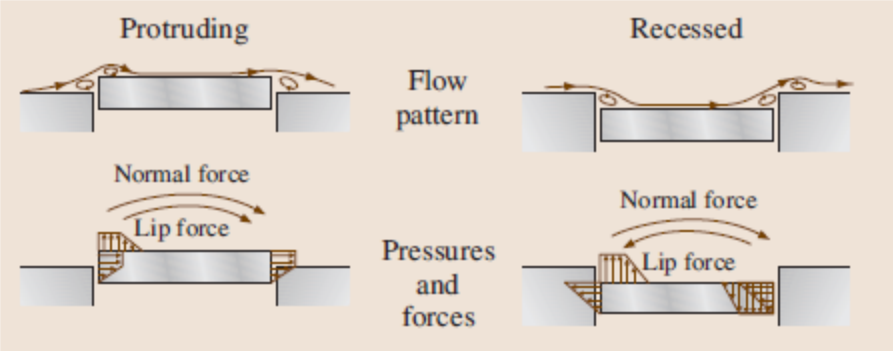

Figure 3: Common placement errors associated with MEMS, obtained from [3], p. 883.

To solve the issues of gaps and misalignment, microfabrication techniques have been implemented [3], [4]. Micro-electromechanical sensors (MEMS) represent a new class of sensors. The use of MEMS-based floating elements can increase spatial resolution because the sensors themselves are smaller and can be placed closer together. This also solves the issue of misalignment, as the MEMS are created monolithically. However, manufacturing and installation of these tiny sensors is challenging, and the end result is still a single point measurement system.

1.1.3. Micro-Electromechanical Sensors

The benefit of MEMS is that their small size allows them to accurately capture the effects of counter-rotating vortex pairs that appear on the surface of a body [7]. MEMS use silicon-based integrated circuit micromachining fabrication techniques, giving increased temporal and spatial bandwidth [4]. MEMS-type sensors can be split into two categories: direct and indirect sensors. The MEMS-type floating element sensor represents the former, while the MEMS-type thermal sensor represents the latter.

Thermal devices work by transducing temperature to voltage [4]. A thin-film sensing element, or "hot-wire" is resistively heated to a temperature higher than that of the surrounding flow. This creates a thermal boundary layer inside the velocity boundary layer. The measured Joulean heating rate is then correlated to shear stress based on a previously established calibration curve.

One such thermal MEMS device consists of vacuum-insulated shear stress sensors with a 300μm pitch and a 30 kHz response time, giving it the necessary spatial and temporal resolution to observe turbulent flow phenomena [7]. Each individual sensor uses the hot-wire technique featuring a polysilicon wire embedded in a nitride diaphragm. A diagram of the sensor is shown in Figure 4. The vacuum cavity allows for better thermal isolation to minimize conductive heat loss [7], [8].

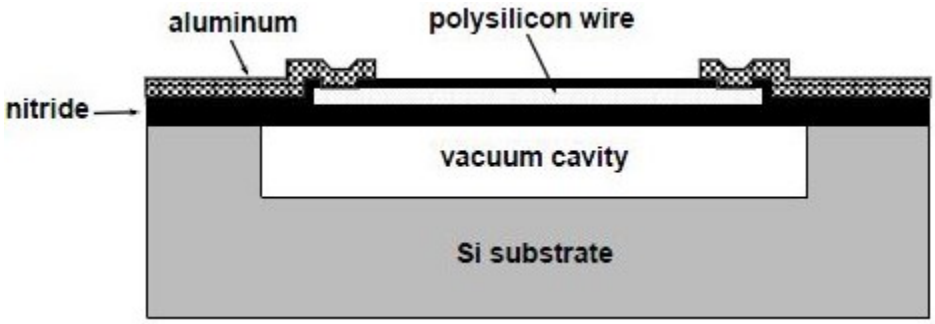

Figure 4: Diagram of hot-wire type MEMS, obtained from [7], p. 2.

A minimum of 25 sensors must be placed in a row, and three rows constitute the imaging chip. The sensors are biased in constant temperature mode and a constant gain set to the output [7]. The constant temperature biasing helps to increase measurement bandwidth [4]. Temperature compensation must be performed to prevent so-called "dc drift." The results of the shear stress tests performed agreed with previously recorded data [7]. Smaller sensors consisting of only 7 hot-wire devices were used by Hites et al, however it was determined that the shear stress measurements provided by these MEMS were insufficient to draw substantial conclusions [8].

While this MEMS has the capacity to be a powerful shear stress sensor, it lacks the simplicity desired in installation. It is also an indirect measure of the shear stress, and therefore requires a number of assumptions in order to calculate the shear stress. Finally, like all previously-discussed shear stress sensors, since it utilizes individual sensors it is still a single point measurement system.

1.1.4. Liquid Crystals – 2D Measurements

Liquid crystals (LCs) are unique substances that can be found in many optical applications. They have many useful properties, and behave in between a solid and a liquid. There exist in nature many different types of liquid crystals, including lyotropic, polymeric, and thermotropic. The discussion here will be limited to thermotropic liquid crystals, as these are not only the most widely used but are the focus of this research. The various liquid crystalline phases in which they can exist are temperature-driven. These phases are referred to as mesophases. Three common phases are nematic, cholesteric, and smectic. These liquid crystals can be thought of as rigid, rod-like structures often consisting of two or more benzene rings connected by linkage groups [9].

The director axis prescribes the imaginary line running along the rigid rod of the liquid crystal. The orientation of the director axis is determined by the mesophase. Figure 5 shows an image of the three aforementioned mesophases in order of structure.

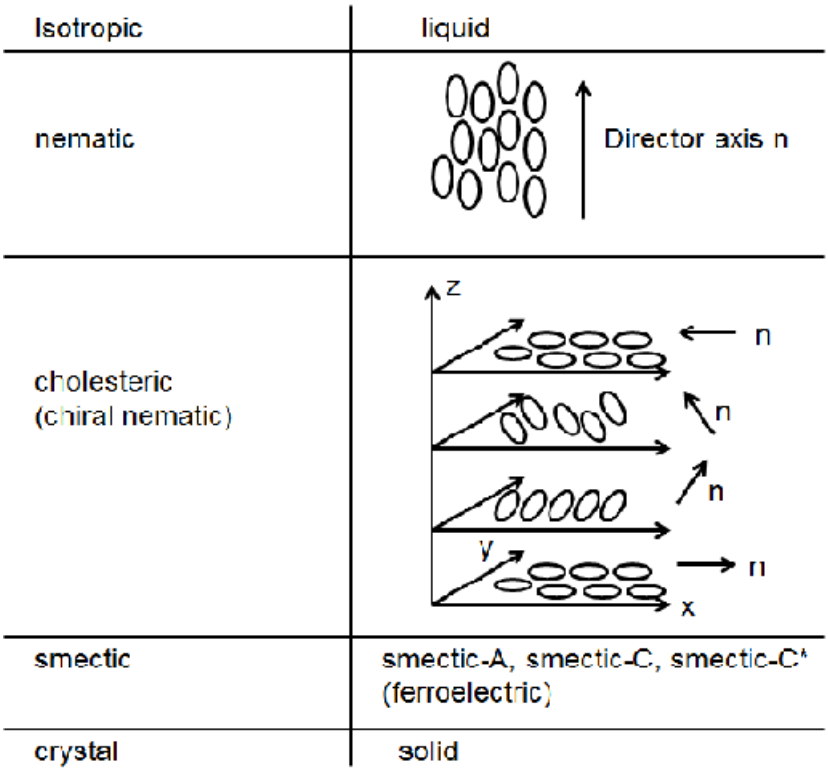

Figure 5: Representation of Common Liquid Crystal Mesophases.

At the top is the pure liquid phase in which the substance is completely isotropic. Slightly more ordered is the nematic phase. In this phase, the director axes of the liquid crystals are aligned in the same direction throughout the liquid crystal. Below the nematic phase is the cholesteric phase, or chiral nematic phase as called when manufactured. In the cholesteric phase there exist planes where all director axes are aligned, just as in the nematic. However, each plane is slightly offset due to the cholesteric liquid crystals having an additional chiral molecule. This results in a helical pattern, as depicted in Figure 5. Of the three mesophases listed, smectic liquid crystals possess the most order to their structure, and are closest to the solid, or crystalline phase. In the smectic phase, the director axes are parallel to one another and perpendicular to the surface [9], [4].

The different mesophases exhibit different optical characteristics. The light scattering properties of the chiral nematic change based on direction and magnitude of an applied shear force. Reda et al. noticed that the pitch of the chiral nematic's helical structure determines the wavelength of scattered light [10]. This led them to use a thin liquid crystal coating to measure the shear force distribution over a sample using a chiral nematic liquid crystal. Figure 6 shows the experimental setup.

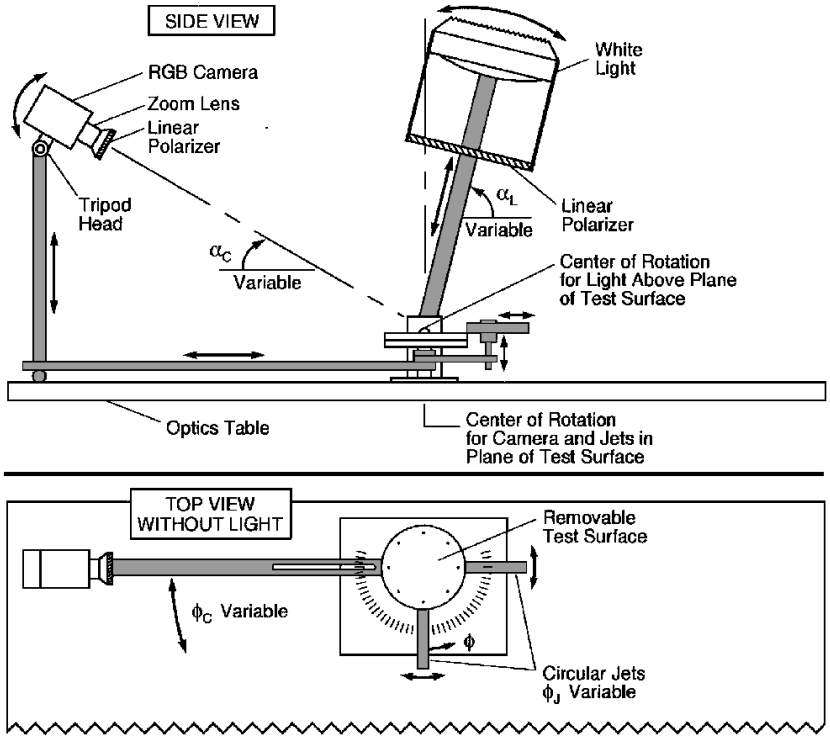

Figure 6: Experimental setup used by Reda et al [11], p. 609.

A white light was shone through a linear polarizer onto the sample while a red-green-blue camera, also with a linear polarizer, observed the sample. The light was set with the angle at 90° so as to strike the surface normal direction, while the camera viewing angle was placed at roughly 30° from horizontal. A turbulent, wall-jet flow was used to generate shear force across the flat sample. This setup was used to obtain a color hue-shear force calibration curve using point measurement techniques. Full-surface images of the LC coating were then taken for multiple in-plane camera angles. A Gaussian curve was fit to the in-plane view angle vs. hue data, and the maximum view angle of the curve-fit determined the vector orientation. The corresponding hue value for this angle was then used along with the calibration curve initially established to determine the shear force. This was repeated for all surface points to give the full-surface vector distribution [11].

The results from the experiment were compared with oil film interferometry measurements and showed good agreement. The largest benefit of the LC coating was the ability to give a full-surface distribution of the shear force. Whereas methods such as OFI and MEMS give only single value measurements, relying on interpolation between points, the liquid crystal coating gave a complete map of exact values, removing the need to interpolate. Another benefit was that the measurements were not limited by the direction of the flow or the orientation of the shear force vector [12]. A drawback of this method is the necessity to repeat measurements for multiple angles due to the fact that the color hue measured is also a function of viewing angle. Furthermore, when using this system with curved surfaces, multiple above-plane angle calibration curves would be needed to account for variations due to surface curvature [11].

Fujisawa et al. demonstrated the use of chiral nematic and cholesteric liquid crystals to measure the shear stress over the curved surface of a NACA0018 airfoil [13]. The number of viewing angles needed for this experiment was only two, down from the seven needed by Reda et al. A calibration curve based on flow over a flat plate was first determined in order to generate shear stress measurements over the curved airfoil. However, this method proved less precise when compared with other liquid crystal methods due to the difficulty of hue measurements.

Buttsworth et al. built off this technique by using nematic liquid crystals in reflective surface measurements to obtain shear stress [14]. Nematic liquid crystals present intensity-based measurements instead of color-based. This reduces the restriction on camera orientation, as the change in measured light intensity is independent of viewing angle.

The use of intensity-based measurements is based on the fact that liquid crystals have two different indices of refraction, one along the director axis and one perpendicular to it. Figure 7 shows the ellipsoid form of the indicatrix, with the difference between the two ellipsoid axes being the birefringence [15]. As the LC layer is sheared, the director axis rotates accordingly. The amount of rotation gives a measure of shear force.

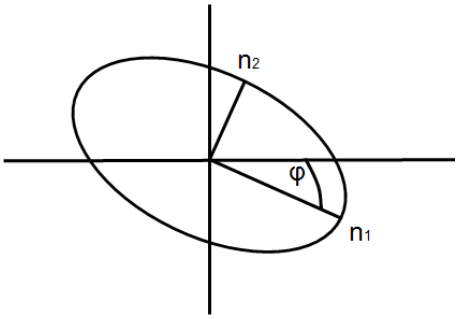

Figure 7: The optical indicatrix.

For the experiments performed by Buttsworth et al. a layer of polyvinyl alcohol (PVA) rubbed with velvet cloth provided a means of pre-aligning the liquid crystals. The application of a shear force would then cause the director axis to rotate, changing the amount of light passing through the LC layer. The experimental setup used by Buttsworth et al. is shown in Figure 8.

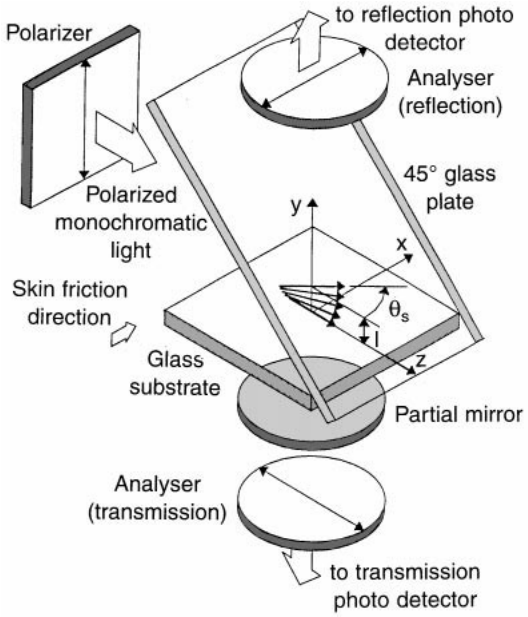

Figure 8: Experimental setup by Buttsworth et al [14], p. 65.

Polarized monochromatic light was reflected off a 45° glass plate to enter the LC layer at a normal incidence. After passing through the LC layer, part of the light was passed through the partial mirror, while the rest of the light was reflected up, enabling both reflective and transmission measurements. In both cases the light was passed through an analyzer before reaching a photo detector, an analyzer being a polarizer placed between the sample and the observer (a "polarizer" is placed between the light source and the sample). A phase difference between the two light rays occurred based on the birefringence.

Certain assumptions had to be made, including that the initial LC orientation (i.e. the rub direction) was perpendicular to the applied shear stress direction, which implies that some previous knowledge of the flow is necessary. Furthermore, there was a time limitation of the test duration to ensure that the LC layer did not flow to the point of a change in layer thickness (while the LC was anchored to the PVA surface, this anchoring was not strong enough to counteract a strong shear force). Furthermore, the technique of measuring changing light intensity through two crossed polarizers gives magnitude information only. A better LC sensor would be a flexible yet well-anchored coating coupled with a measurement system for both magnitude and direction of the shear force.

1.2. Polymer-Dispersed Liquid Crystals

The ideal sensor would allow for repeatable measurements. In other words, the sensor should return to zero when the shear force is removed. To accomplish this, the liquid crystals are placed within a polymer matrix, creating what is known as a polymer-dispersed liquid crystal, or PDLC. In a PDLC, the liquid crystals are confined to droplets within the polymer. In the absence of an externally applied force, the droplets assume a random orientation. Light shining through the sample encounters many different indices of refraction from the polymer and from the many orientations of the liquid crystal director axes and is therefore scattered. The PDLC appears opaque, or "milky white" to the observer. When an external force is applied, such as an electric field or a shear force, the liquid crystals orient themselves in the same direction. The indices of refraction between the liquid crystals along their director axis and the polymer match, the PDLC appears transparent, and the light is able to pass through [16], [9]. A simple schematic of this is shown in Figure 9. The elasticity of the polymer allows for the PDLC to return to a

relaxed state once the force is no longer being applied based on surface interactions at the droplet wall and the non-ideal spherical shape of the droplets [17]. This results in a nominally reversible sensor [16], [18].

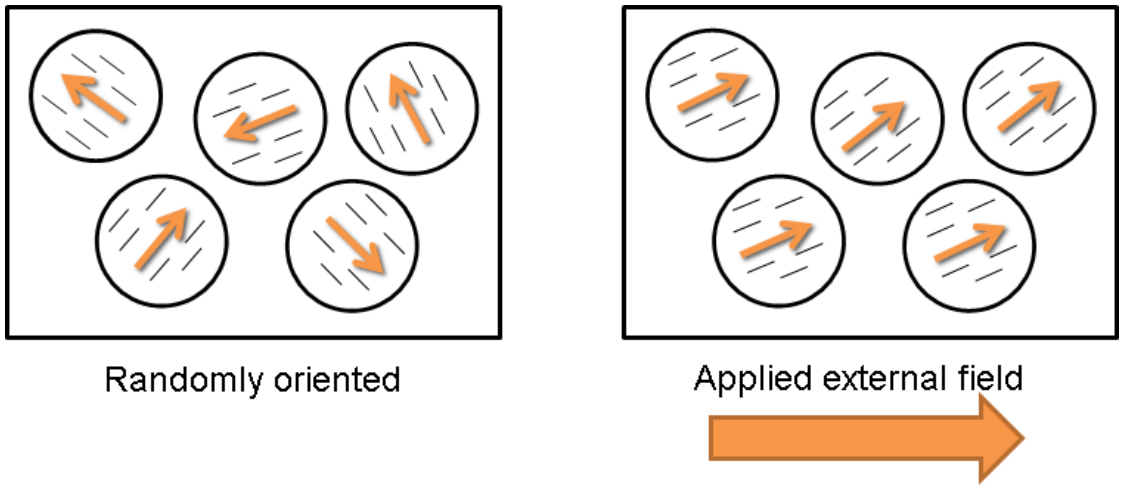

Figure 9: PDLC schematic showing (left) absence of applied field and (right) presence of applied field.

The polymer for the PDLC should be chosen such that its index of refraction matches the liquid crystal index of refraction along the director axis, which typically ranges from 1.48 to 1.54. This ensures that, as the liquid crystals align themselves to the polymer, the light passing through the sample encounters closer indices of refraction, and thus more light is allowed through. Thus the birefringence itself becomes a measure of the applied shear force. Several additional considerations must be made when selecting a polymer. The chosen polymer should be highly transparent with no light-scattering effects, as this detracts from the liquid crystal's scattering abilities. The polymer should have good film-formation abilities and should adhere well to the support structure. The polymer should have good mechanical properties, such as high elasticity and low brittleness. The polymer must be chemically inert to the liquid crystal, as this helps ensure purity of the liquid crystal droplets. While it is desirable to have high miscibility between the liquid crystal and liquid polymer, it is undesirable to have contamination of the solid polymer by the liquid crystal. However, in the cases of most PDLCs, some contamination does occur, resulting in slight changes of physical properties such as the refractive index or the glass transition temperature [17].

Different droplet configurations are possible based on the surface anchoring of the liquid crystals within the droplet, as well as the droplet size and density [19]. The polymer used plays a large impact in determining the stresses present, which in turn dictates the specific shape of the droplets. The droplets themselves can be easily viewed through crossed circular polarizers using a microscope. A sample of radial droplets at 14x magnification is shown in Figure 10. These represent the liquid crystal islands, made up of multiple liquid crystal molecules, within the polymer matrix.

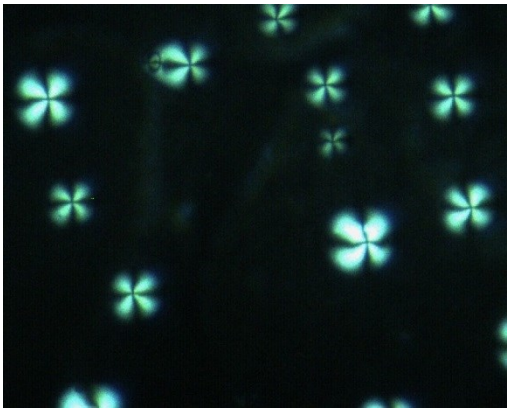

Figure 10: Radial droplets viewed at 14x magnification.

Previous research has proven the feasibility of the PDLC shear sensor, as well as the many benefits it has over conventional shear force measurement systems as well as other liquid crystal measurement systems. The use of a partially-exposed PDLC coating has shown a change in light intensity when viewed through crossed polarizers [18]. The change in director axis orientation was shown to be linear with respect to the change in applied differential pressure. These results were observed under a microscope using polystyrene and a nematic liquid crystal.

1.3. Birefringence Measurement

By measuring the intensity of light through the sample in the presence of a shear force and relating that back to an initial light intensity measurement, the birefringence of a sample can be calculated. Wood and Glazer [20] proposed a method to achieve this using the combination of a quarter wave plate and a linear polarizer to create a circular polarizer. Figure 11 shows how

unpolarized light passed through a linear polarizer at a 45° angle and a quarter wave plate results in circularly polarized light.

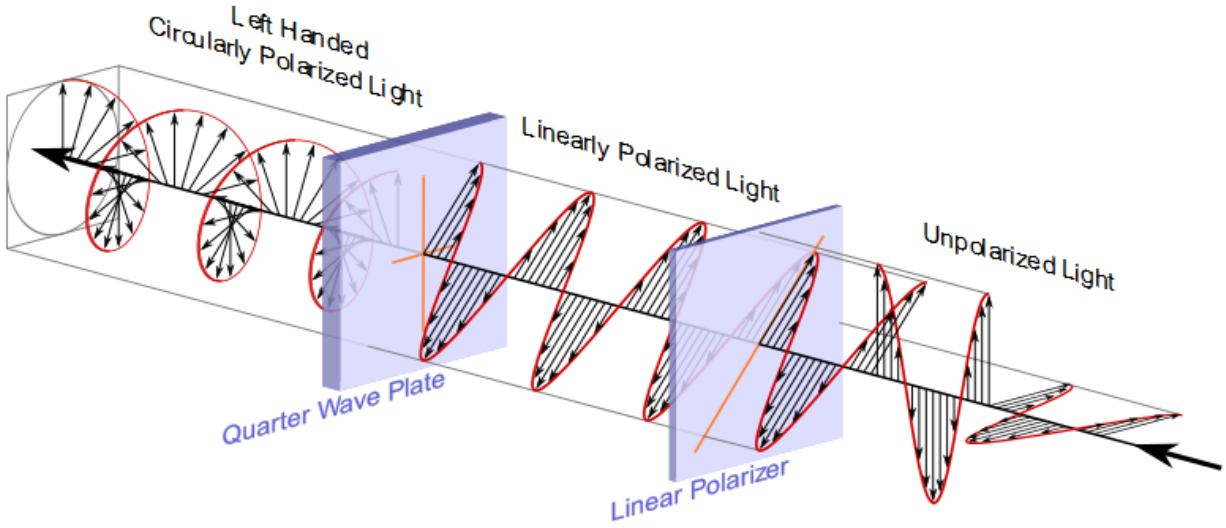

Figure 11: Unpolarized light becoming circularly polarized, obtained from [21].

Circularly polarized light that is passed through a birefringent surface will then become elliptically polarized. The light is then passed through a linear analyzer that rotates with a frequency ω. The measured intensity is then given by Equation 1, where I_0 is the initial intensity, t is time, and δ is the phase shift given in Equation 2, where λ is the wavelength of light, Δn is the birefringence, and L is the material thickness. As seen in Figure 7, φ is the angle between the horizontal and the larger index of refraction, referred to as the extinction angle [15].

$$I = \frac{1}{2} I_0 [1 + \sin[2(\omega t - \varphi)] \sin \delta] \quad (1)$$

$$\delta = \frac{\pi}{\lambda} \Delta n L \quad (2)$$

The birefringence Δn is a sinusoidal function of the difference in indices of refraction of the liquid crystal, as seen in Equation 3, where n_e and n_o are the extraordinary and ordinary indices of refraction, respectively, and θ is the angle between the liquid crystal director axis and the substrate normal [22].

$$\Delta n \approx (n_e - n_o) \sin^2 \theta \tag{3}$$

By taking the intensity measurements at N discrete angles, ωt is replaced by α_i, as seen in Equation 4, where α_i are the angles used, i ranging from 1 to N [23]. This removes the need to use a continuously rotating polarizer.

$$I_i = \frac{1}{2} I_0 [1 + \sin[2(\alpha_i - \varphi)] \sin \delta] \tag{4}$$

Equation 4 can be linearized into Equation 5 using a trigonometric conversion, where a_0, a_1, and a_2 are given in Equation 6 [23].

$$I_i = a_0 + a_1 \sin 2\alpha_i + a_2 \cos 2\alpha_i \tag{5}$$

$$a_0 = \frac{1}{2} I_0, \quad a_1 = \frac{1}{2} I_0 \sin \delta \cos 2\varphi\,, \quad a_2 = -\frac{1}{2} I_0 \sin \delta \cos 2\varphi \tag{6}$$

The linearization removes the need for explicit matrix inversion, as the system of equations becomes diagonal when intensities are measured for angles $2\alpha_i$ covering the full period of the sinusoidal functions. Equation 6 can then be rewritten in terms of the measured intensity, as seen in Equation 7 [23]. A detailed explanation of the derivation utilizing the least-squares method is given in Appendix B.

$$a_0 = \sum_{i=1}^{N} \frac{1}{N} I_i, \quad a_1 = \sum_{i=1}^{N} \frac{2}{N} I_i \sin 2\alpha_i\,, \quad a_2 = \sum_{i=1}^{N} \frac{2}{N} I_i \cos 2\alpha_i \tag{7}$$

Kaminsky proposed the use of four angles ranging from 0° to 135° in 45° increments [23]. Setting the α_i values to 0°, 45°, 90°, and 135°, Equation 7 can be rewritten as Equation 8 [23].

$$a_0 = \sum_{i=1}^{4} \frac{1}{4} I_i, \quad a_1 = \frac{1}{2}(I_2 - I_4), \quad a_2 = \frac{1}{2}(I_1 - I_3) \tag{8}$$

The four intensities come from the four measured intensities at the corresponding angles. The birefringence then becomes a function of the phase shift only, and is proportional to $|\sin\delta|$, which is given in Equation 9 [23].

$$|\sin\delta| = \frac{1}{a_0}\sqrt{{a_1}^2 + {a_2}^2} \tag{9}$$

Thus it can be shown that using only four angles the birefringence of a sample can be measured. Furthermore, the extinction angle can be calculated as in Equation 10.

$$\varphi = \frac{\pi}{2} + sgn(a_2)\frac{1}{2}\cos^{-1}\left(\frac{-a_1}{\sqrt{{a_1}^2+{a_2}^2}}\right) \tag{10}$$

The transmittance of the sample is simply given by a_0. As seen in Equation 8, a_0 computes the averaged light intensity across the four angles. This value is also needed to make the birefringence and extinction angle independent of light intensity, and the signal to noise ratio is improved by 10 to 100 times compared with the rotating polarizer approach.

The benefit of this method is that all measurements are done in real time. Furthermore, information regarding both the magnitude and the direction of the shear force is available.

1.4. Production Methods

There are three common methods for the creation of PDLC: solvent-induced phase separation (SIPS), polymerization-induced phase separation (PIPS) and thermally-induced phase separation (TIPS) [24], [25], [26], [17].

In the SIPS method, the polymer and liquid crystal are mixed with a solvent. When enough solvent is present, the interaction energies between the polymer and the solvent and the liquid crystals and the solvent become dominant. Both of these interaction energies are negative, resulting in a negative or small positive value for the interaction energy of the homogenous form. As the solvent evaporates, the interaction energy between the polymer and the liquid crystal becomes dominant. As this interaction energy is positive, the homogenous interaction energy becomes large and positive, leading to a positive free energy. Phase separation occurs as a result,

and liquid crystal droplets are formed until polymer gelation occurs. The evaporation rate of the solvent determines the size and density of the droplets. Proper control of the solvent evaporation rate is critical in producing uniform specimens.

The PIPS method is useful when low molecular weight LCs are being used in conjunction with prepolymers [17]. In this method, liquid crystal is combined with a monomer or prepolymer, which is then polymerized at a fixed temperature. The degree of polymerization of a monomer is 1 (the lowest value). The liquid crystal and monomer exist in a homogenous mixture due to the negative free energy and large mixing entropy. As the degree of polymerization increases, the mixing entropy decreases, the free energy increases, and the liquid crystals phase separate [24]. Liquid crystal droplets begin to form, and continue to do so until polymer gelation occurs [17]. At this point the liquid crystal droplets begin to purify as the polymerization continues. This results in an increase in the nematic-to-isotropic phase transition temperature and may be the result of a molecular transfer process [26]. There are two types of polymerization: thermally-induced or photo-initiated. In thermally-induced polymerization, the monomers are typically epoxy resins that are cured at an elevated temperature. A higher temperature or higher concentration of epoxy resins increases the reaction rate, which in turn leads to smaller droplets. Thus the cure temperature plays a critical role in droplet size. In photo-initiated polymerization, photo-initiators and monomers with acrylate or methacrylate end groups are used. Higher UV irradiation leads to smaller droplets [24].

In the TIPS method, the phase separation of the system is the result of a temperature decrease, and is best for use with thermoplastics that melt below their decomposition temperature [17]. The goal is to make the interaction energy between polymer molecules and liquid crystal molecules higher than the average interaction energy between two polymer molecules or two liquid crystal molecules. When this is the case, the mixture exists in a homogenous form. An increase in temperature leads to higher entropy; the homogenous phase represents the lower free energy and the system moves towards homogeneity. A decrease in temperature decreases the mixing energy, resulting in phase separation, liquid crystal droplet formation and polymer gelation. The cooling rate of the polymer controls the droplet size, with a faster rate resulting in smaller droplets. This is due to the fact that a longer cooling time gives more time for phase separation, droplet growth, and droplet coalescence. The droplet diameter directly influences the

optoelectronic properties of the PDLC [26]. This method generally requires a larger concentration of liquid crystals than the PIPS method [17].

In general, most thermoplastic polymers and liquid crystals won't mix at room temperature. A solvent can therefore be used first to mix the liquid crystal and the polymer. Once the solvent is evaporated, the PDLC coating is heated and cooled, leading to phase separation. This process may be repeated multiple times to generate different droplet sizes [24].

Over time, the number of liquid crystal droplets present in the PDLC decreases while the size of the droplets increases. This is a result of the coalescence of the liquid crystal droplets [25]. Furthermore, a higher concentration of liquid crystals produces fewer and smaller liquid crystal droplets within the polymer matrix.

1.5. Objectives

The current research has three main objectives: the use of PDLC shear sensors using reflective measurements, the use of PDLC shear sensors over a larger surface area, and the use of PDLC shear sensors on a flat boundary layer.

1.5.1 Reflective Mode

Previous tests required a light to be shined through a glass sample. Future applications in wind tunnel testing would most certainly be using opaque test samples. It was therefore imperative to create a method by which data could be collected via reflection. Different reflective surfaces would need to be analyzed to see which gave the best signal. Another concern is whether the polarization of the light would be preserved after reflection. This is based on the reflective material itself, and whether direct reflection or diffuse reflection was occurring.

1.5.2 Larger Area

Previous tests had been done using small samples and viewing small areas. Future applications in wind tunnel testing would most certainly require the viewing area to be much larger in order to gain any insightful information. Special care would need to be taken in order to ensure that the larger area was fully illuminated. Furthermore, a different lens would be

needed to give high resolution over a larger area. The system resolution would need to give consistent values between the different viewing area sizes.

1.5.3 Flat Boundary Layer

To generate a smooth, laminar boundary layer, an aluminum wedge shall be used, as the sharp blade-like leading edge of the wedge will produce a smooth boundary layer.

Chapter 2. Experimental Setup

A variety of setups were used during the course of this research. The two modes discussed below, transmission mode and reflective mode, refer to the setup of the light source. Two additional categories can be considered based on the equipment. A portion of the testing was done in the wind tunnel, but the majority of the testing was done using what is referred to as the calibration setup.

In all setups, the light was passed through a diffuser and a circular polarizer before passing through the sample and into the camera setup. The circular polarizer consists of a linear polarizer and a quarter wave plate attached together at an angle optimized for 570nm wavelength light. The birefringence measurement was done using the QuadView system by Optical Insights. A schematic of this system is shown in Figure 12. The light from the sample encounters the beam splitter and is split and reflected up through linear polarizers to the CCD chip and the camera.

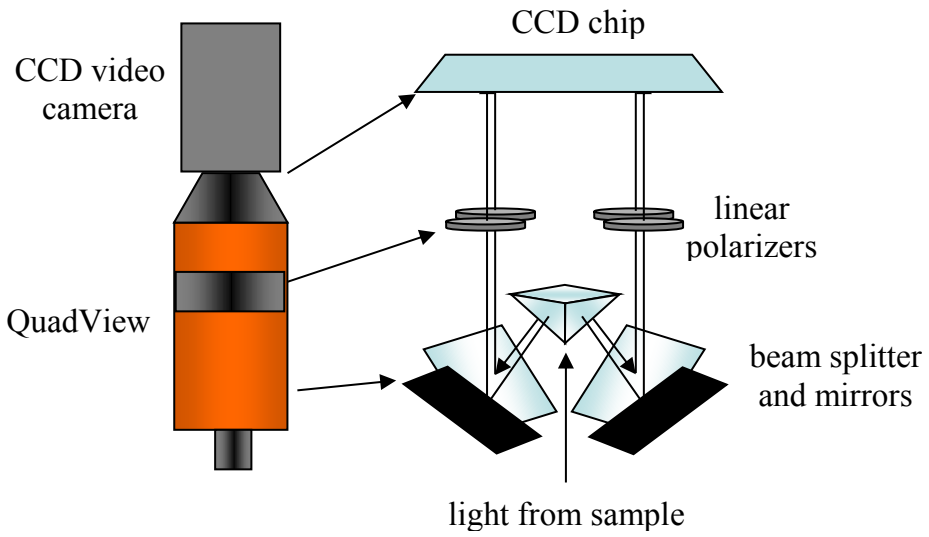

Figure 12: Schematic of QuadView system.

The camera used was an AmScope MD800 CCD camera connected to the computer via USB. The majority of the tests were done using a Comiscar 16 mm lens, while the final tests were done using a Computar ½in 4-8mm megapixel lens to achieve the desired level of zoom for viewing the larger area.

For wind tunnel testing, a Jet Stream 500 wind tunnel was used. The wind tunnel featured a proportional-integral-derivative (PID) controller to activate a 1hp AC motor. The wind tunnel speed could vary between 0 and 80mph. The test chamber measured 5.25in by 5.25in and was sealed with thick annealed glass. A pitot tube was positioned to the side of the flow so as not to obstruct the flow with its measurement. The test pieces were clamped into place along the floor of the test section, and the test section floor locked in the test section. Large C-clamps helped prevent the structure from vibrating during testing. The QuadView-camera system was supported on a metal structure next to the test section and bolted in place to prevent vibrations.

For calibration testing, a shear force was applied via a top slide while the lower slide was held in place. Fishing line was taped to the top slide, draped over a small pulley, and attached to small weights. The entire setup was placed on top of a glass plate to allow light to shine through. The QuadView-camera system was clamped to a metal pole so as to point down towards the sample.

2.1 Transmission Mode

In transmission mode, the light source shone through the glass sample. For these tests, light was provided by a Lumitex, Inc. dual-port source powered by a 21V, 150W halogen lamp. For the wind tunnel setup, the lamp sat opposite the QuadView setup. A schematic is shown in Figure 13.

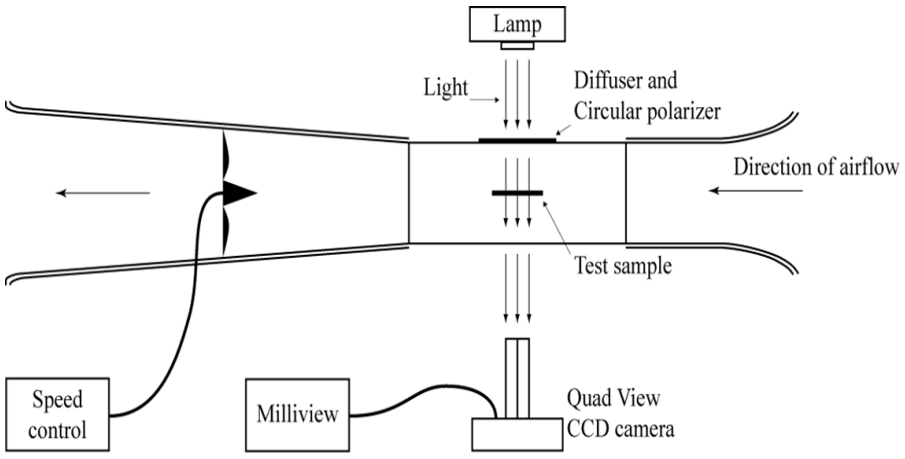

Figure 13: Schematic of wind tunnel setup in transmission mode.

In the calibration setup, the light was placed below the glass table so as to shine up through the slide and into the QuadView setup. A simple schematic is shown in Figure 14.

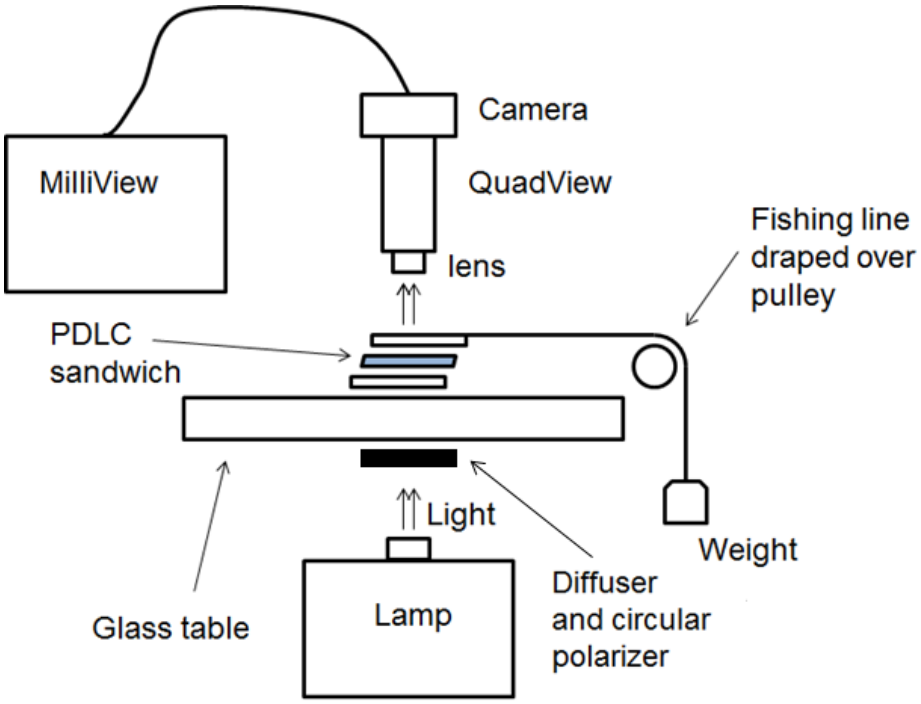

Figure 14: Schematic of calibration setup in transmission mode.

The Comiscar lens was used for both setups, giving a viewing image of roughly 25mm x 25mm, or the width of the slide.

2.2 Reflective Mode

In reflective mode, the light source needed to pass through the sample and be reflected back to the camera. This required that the light be offset at a slight angle. The halogen lamp previously used was too heavy to be efficiently incorporated into the reflective setup. As a result, different light sources were used. For the calibration setup, a General Success Model GS-T00555 LED 10.5V, 0.5A lamp was used. A schematic of the calibration setup in reflective mode is shown in Figure 15.

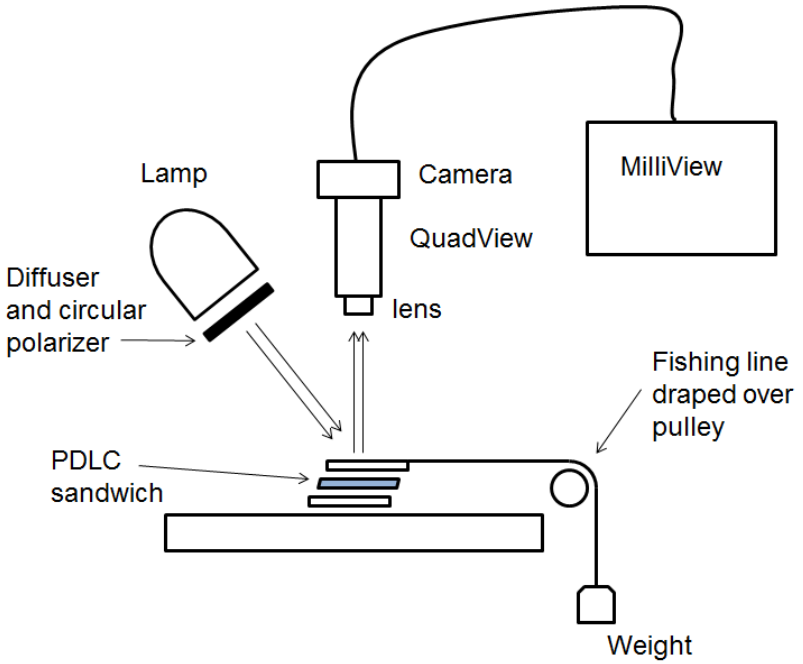

Figure 15: Schematic of calibration setup in reflective mode.

It however proved too dim to sufficiently illuminate the samples within the wind tunnel. A similar goose-neck desk lamp with a clamp fitted with a 60W LED flood bulb was used for the wind tunnel setup. As the LED bulb was equipped with a diffuser plate, the additional diffuser plate attached to the circular polarizer was removed. In order to have high enough signal strength, a lens was used in order to focus the light. A schematic of the wind tunnel setup is shown in Figure 16.

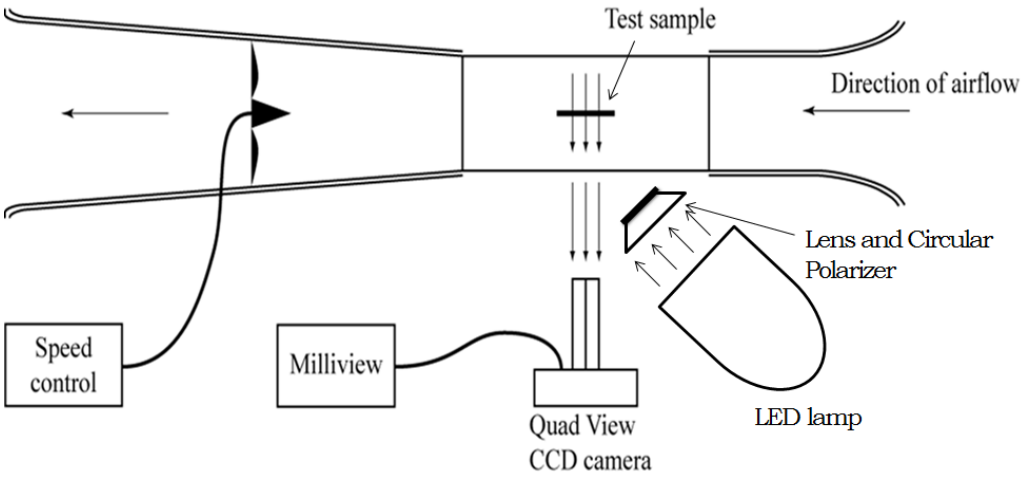

Figure 16: Schematic of wind tunnel setup in reflective mode.

To achieve the reflective background, a silver spray-painted slide was placed behind the slide being tested. More information regarding the various reflective backgrounds tested can be found in Section 3.4.

2.3 PDLC Preparation

Unless otherwise specified, the slides were all created using the nematic LC E7 purchased from Jiangsu Hecheng Display Technology Co. LTD and LCR HallCrest, Inc. The polymer most commonly used was polymethylmethacrylate, or PMMA. Two different molecular weights, 25,000 and 75,000, were purchased from Polysciences, Inc. The solvents used were dichloromethane (DCM) and toluene.

A combination of SIPS and TIPS methods were used to create the PDLC samples used. To create the PDLC, 0.5g of polymer was mixed with 10mL of solvent. In most cases, the solvent was 90% DCM with 10% toluene added to slow the curing rate and ensure that the polymer did not fully cure before reaching the glass slide. Once the polymer was fully mixed, a portion was removed and combined with liquid crystals in a 1:2 ratio. The next day the PDLC was airbrushed onto 25mm x 75mm glass slides at a pressure of 20 psig and a spray distance of roughly 3in. For tests done with the calibration setup, a second glass slide was placed on top of the first to create a sandwich. The solvent was evaporated from the slide, and then the slides were placed in the oven at 80°C for one hour. The slides were then allowed to cool to room temperature. This method, used with PMMA, created very small droplets of a bipolar configuration [24], [16]. For tests done with the wind tunnel setup, the slide was allowed to dry for at least one hour before being tested, and no heating was performed. For the final test in reflective mode, an aluminum wedge was used, measuring roughly 9.5cm wide and as tall as the test section. The wedge was first coated with silver spray paint to make a more uniform reflective surface before receiving a coating of PDLC.

2.4 Testing Procedure

The same procedure was used for all tests with the same equipment. For the wind tunnel testing, tests were conducted at 20mph increments up to 80mph. After each test point, the wind was turned off and the system allowed to return to equilibrium. Data points were collected at

wind-on and wind-off points. Three points were taken for each speed point, and the average of the three used as the final value. Error bars were given by the standard deviation between the three points.

For the calibration setup, the mass was added in 10g increments up to 80g. Unlike the wind tunnel testing, the mass was not removed in between data points.

The MilliView software designed by Werner Kaminsky was used to collect birefringence data. Figure 17 shows a screenshot of the MilliView software, taken before the start of a test. Before beginning testing, a background check would be performed to set the initial birefringence to nominally zero. Throughout the test, the birefringence, extinction angle, and intensity change data were visible. Color-coded bars indicated the relative values, while clicking and dragging a box over the image gave the exact average value.

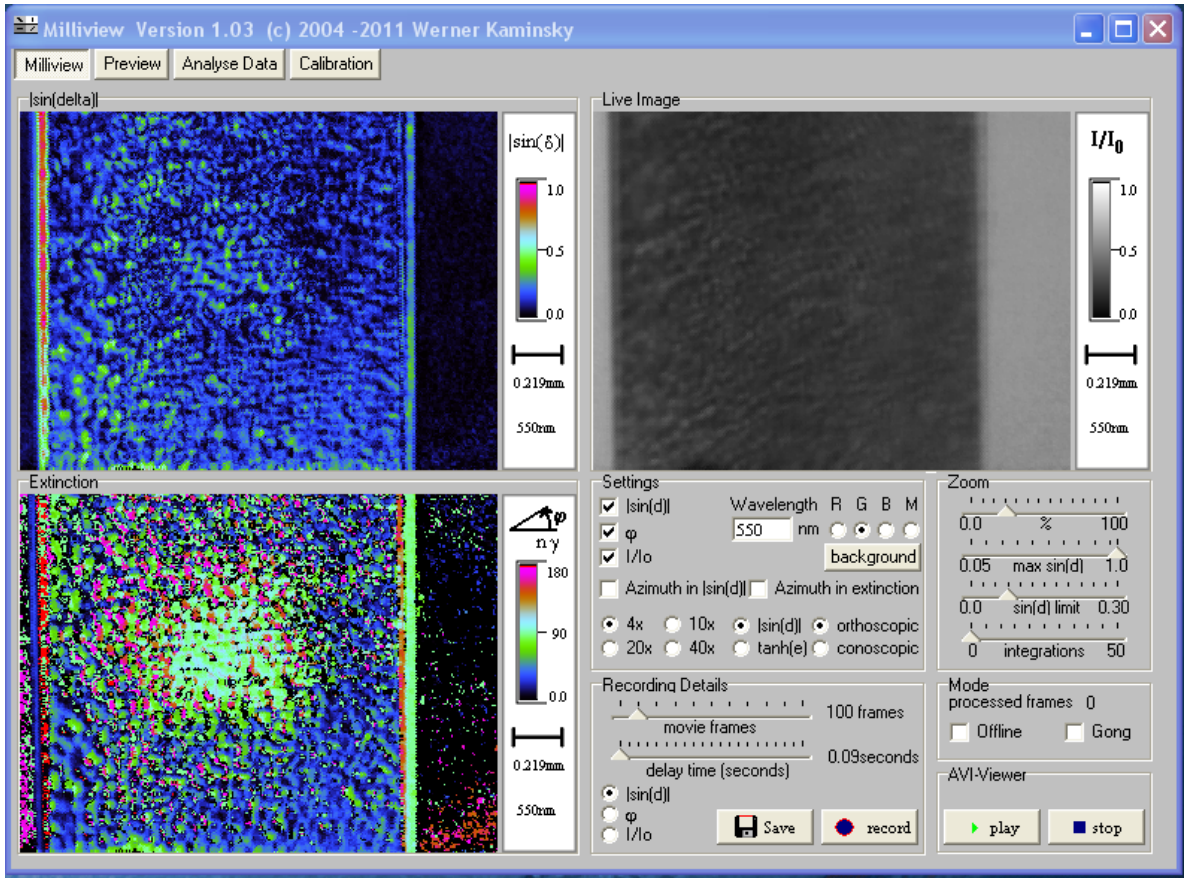

Figure 17: Screenshot of MilliView software.

Before each test a careful calibration of the four images was performed to ensure that the MilliView software was correctly aligning the four images. A simple saturation check was also performed using the live image provided by MilliView. This image was fed into Matlab and the green pixel intensity values were checked to make sure that less than 1% was at 255, i.e. saturation. A visual check was also performed to make sure that the sample was fully illuminated. This was verified by the background check on the sample showing zero birefringence.

Most tests used live data recording, but in the case of the wedge images of the birefringence were saved and analyzed using MilliView's "Analyse Data" function. This was to ensure that locations used for birefringence readings were the same for all speed points.

2.5 Calculations

To assess the validity of the system as a shear force measure, the wind tunnel data was compared to a calibration curve developed based on knowledge of shear stress. The shear force is measured by the change in birefringence, which is itself a function of the change in director axis orientation θ. The change in director axis is related to shear strain according to Equation 11.

$$\theta = \frac{1}{2}\gamma \tag{11}$$

The shear strain is related to the shear stress and the shear modulus as seen in Equation 12 [27].

$$\gamma = \frac{\tau}{G} \tag{12}$$

Plugging Equations 2, 3, and 13 in to the function for birefringence yields birefringence as a function of shear stress.

$$|\sin\delta| = \left|\sin\left[\frac{\pi}{\lambda}(n_e - n_o)L\sin^2\left(\frac{1}{2}\frac{\tau}{G}\right)\right]\right| \tag{13}$$

The shear stress is related to wind velocity via the coefficient of skin friction and the dynamic pressure [28].

$$C_f = \frac{\tau}{\frac{1}{2}\rho U^2} \tag{14}$$

The coefficient of skin friction is also related to the Reynolds number, given in Equation 15, where ρ is the density of air, x is the position from the leading edge, and μ is the kinematic viscosity [28].

$$Re_x = \frac{\rho x U}{\mu} \tag{15}$$

The relationship between skin friction and the Reynolds number varies depending on whether the flow is turbulent or laminar. Equations 16.a and 16.b show the skin friction coefficient for turbulent and laminar flows, respectively [28].

$$C_f = \frac{0.0583}{Re_x^{0.2}} \tag{16.a}$$

$$C_f = \frac{0.0664}{\sqrt{Re_x}} \tag{16.b}$$

Using Equations 14, 15, and 16, the shear force can be rewritten as a function of wind velocity and location.

$$\tau = 0.0291\rho^{0.8}\frac{\mu^{0.2}}{x}U^{1.8} \tag{17.a}$$

$$\tau = 0.332\sqrt{\frac{\rho\mu}{x}}U^{1.5} \tag{17.b}$$

Plugging Equation 17 in to Equation 13 then gives birefringence as a function of wind speed for either turbulent or laminar flow.

Chapter 3. Results

The following section details the various tests conducted. Unless otherwise specified, all tests were done using PMMA and E7 in a 1:2 ratio.

3.1 PMMA Molecular Weight Study

A brief study was conducted using the two different molecular weights of PMMA. It was predicted that the lower molecular weight PMMA would show a larger maximum birefringence value. This was first confirmed in a transmission-mode wind tunnel test, the plot of which is show below in Figure 18. As shown in the plot, the difference between peak birefringence values is almost doubled between the two molecular weights. As expected, the higher molecular weight PMMA was stiffer. This could prove useful in situations where a highly sensitive sensor is needed in one area while a lower sensitivity sensor is needed in another section of the test part as a result of different stress intensities.

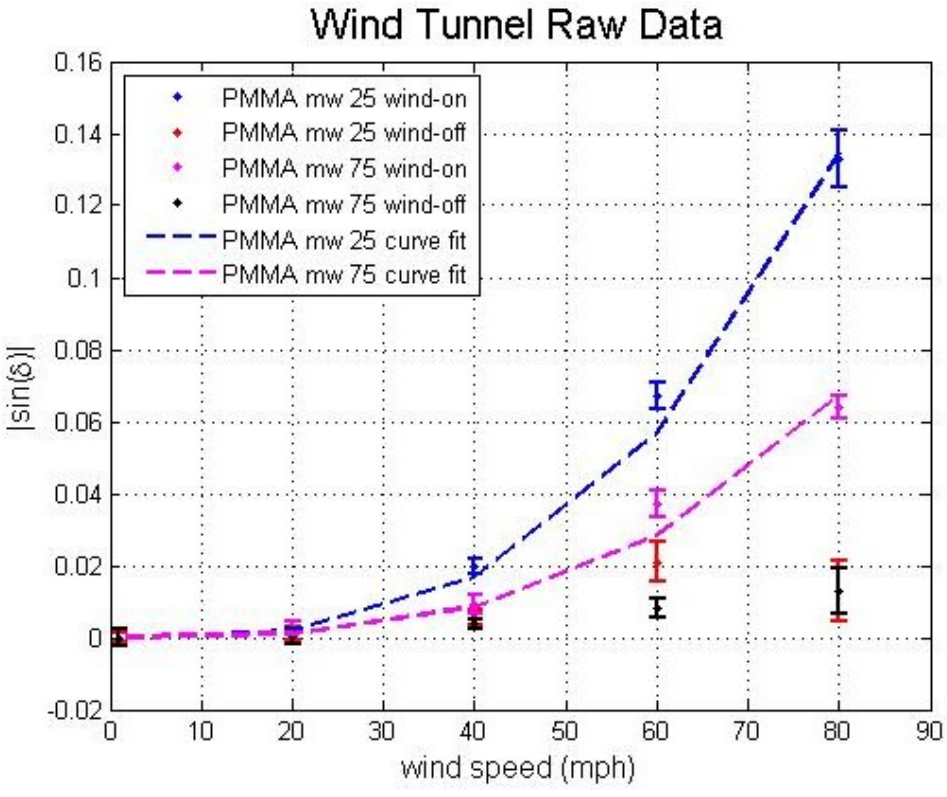

Figure 18: Comparison of different molecular weight PMMAs in wind tunnel.

The test was conducted using four slides of each polymer. Each slide was tested at the four speed points. In between the speed points, the wind tunnel was turned off and the wind-off value taken. Each data point is the average of the three values taken for all four slides, and the error bars represent one standard deviation for all twelve data points.

A curve fit based on Equation 13 was applied to wind-on data. This curve assumed the laminar model expressed in Equation 17.b based on the calculated Reynolds number being lower than the critical number for a flat plate [29]. The unknown constants were set based on assumed PDLC thickness and the highest R-squared value when compared with the wind tunnel data. The lower molecular weight had an R-squared value of 0.991 while the higher molecular weight had an R-squared value of 0.9717.

The PMMA comparison was repeated using the calibration setup. This test was originally performed by Fletcher to validate that the birefringence was a measure of shear force [30]. As a result, the data should be linear, hence the use of a linear curve fit. Figure 19 shows the results of the test. The test was conducted in a similar manner as the wind tunnel PMMA test, and the error bars represent the standard deviation for the average of the three data points. The R-squared value for both molecular weights is 0.9923.

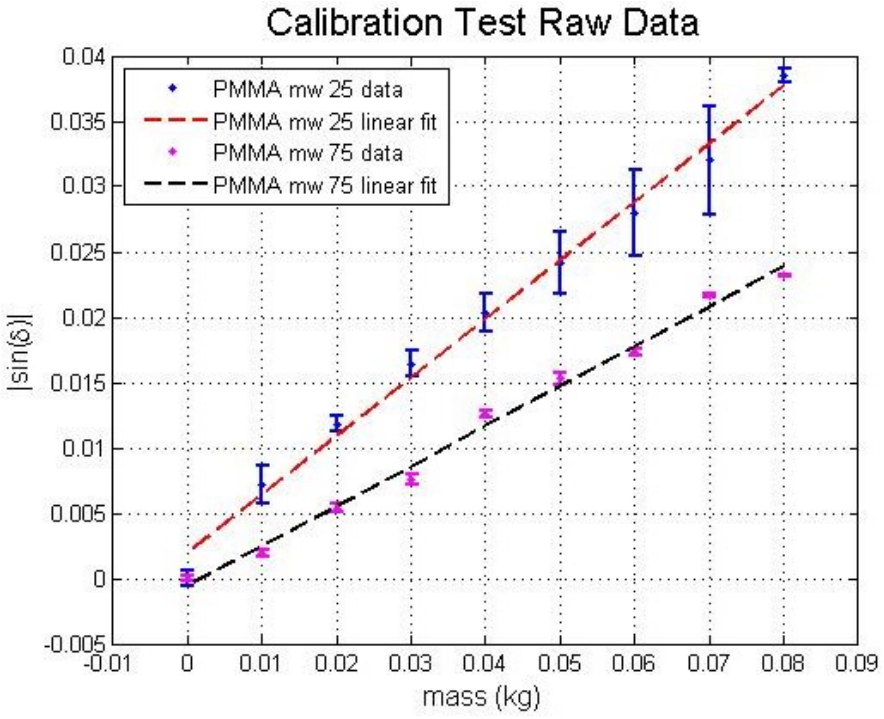

Figure 19: Comparison of different molecular weight PMMAs in calibration test.

As in the case of the wind tunnel test, the lower molecular weight showed higher birefringence values. This test also confirmed that the PDLC worked as a shear sensor outside of the wind tunnel.

The next step was to then compare the data taken from the wind tunnel with the data taken in the calibration test. Both data sets were plotted as birefringence versus shear stress. The mass was converted to shear force by simply multiplying by gravitational acceleration and dividing by the area of the 25 x 75 mm glass slide. For the wind tunnel calculation, the variable coefficient was changed based on the relationship between shear stress and the turbulent coefficient of stress.

Figure 20 shows the plots for the two molecular weights comparing the calibration data versus the wind tunnel data. The same error bars are used. To show the direct comparison, the calibration data were scaled to plot against the wind tunnel data. However, the calibration data spanned a shear stress from 0 to roughly 400 Pa, while the wind tunnel stress was less than 0.5 Pa.

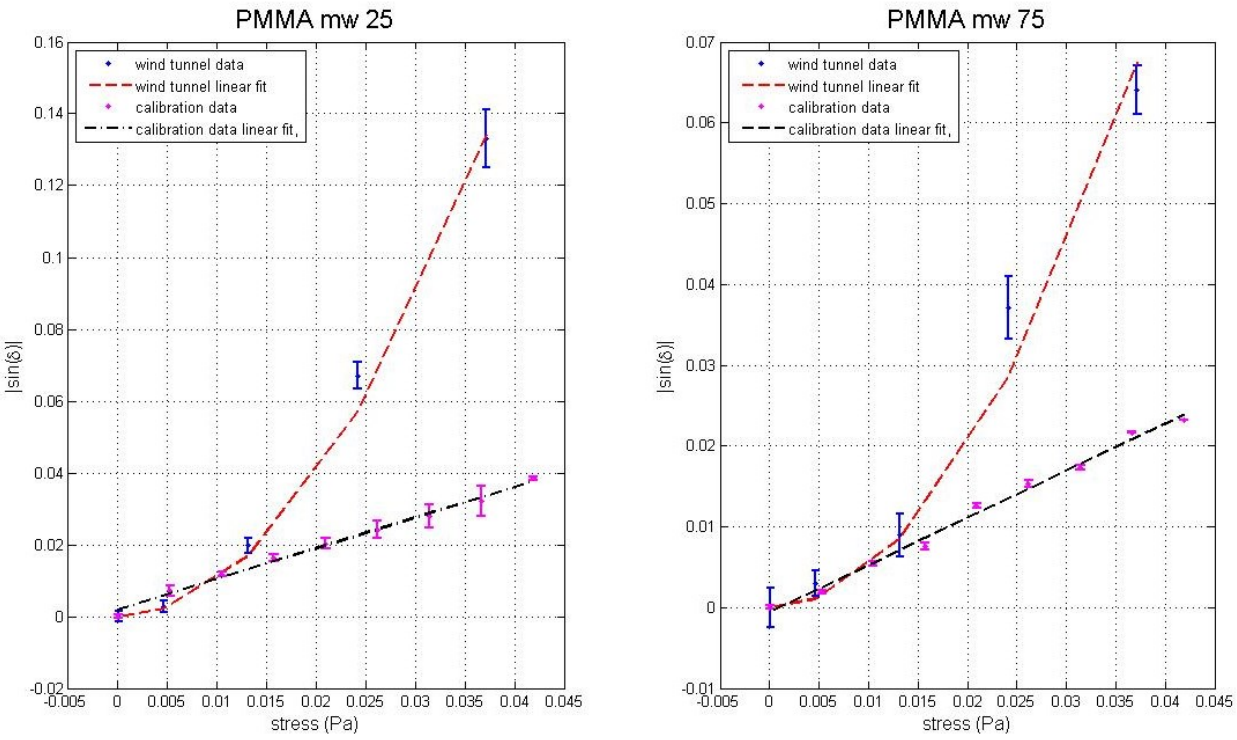

Figure 20: Comparison of wind tunnel versus calibration test data.

Figure 21 below shows the comparison by test type, with both molecular weights plotted together. The same trend is visible in both the wind tunnel data and the calibration test data, namely that the lower molecular weight PMMA displayed a higher birefringence compared to the higher molecular weight.

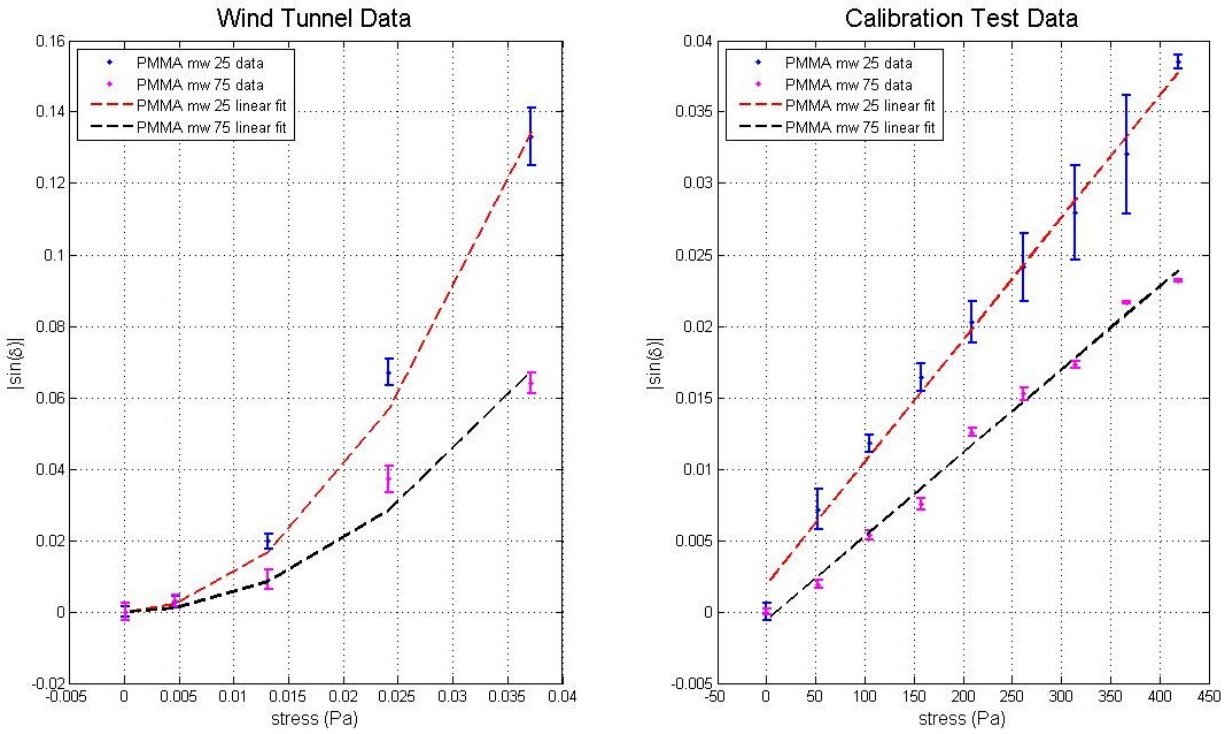

Figure 21: Side-by-side comparison of PMMA by molecular weight

3.2 Annealing

The process of annealing involves heating the test sample up to a specific value so that the polymer becomes fluid again. This allows the polymer to flow and can reduce any stresses that occurred during the initial cure process. Heating the PDLC also helped with the phase separation, as previously mentioned. Two studies on the effects of annealing were performed using the wind tunnel setup and the calibration test setup. In the wind tunnel setup, annealed slides were compared with non-annealed slides using both molecular weights of PMMA. The results are shown in Figure 22. The annealed slides were sprayed like usual and then placed in the oven at 80°C for one hour. The wind tunnel was run at speeds of 0 to 80 mph in 13 mph

increments. Values were taken for wind-on and wind-off conditions, although only the wind-on conditions are plotted.

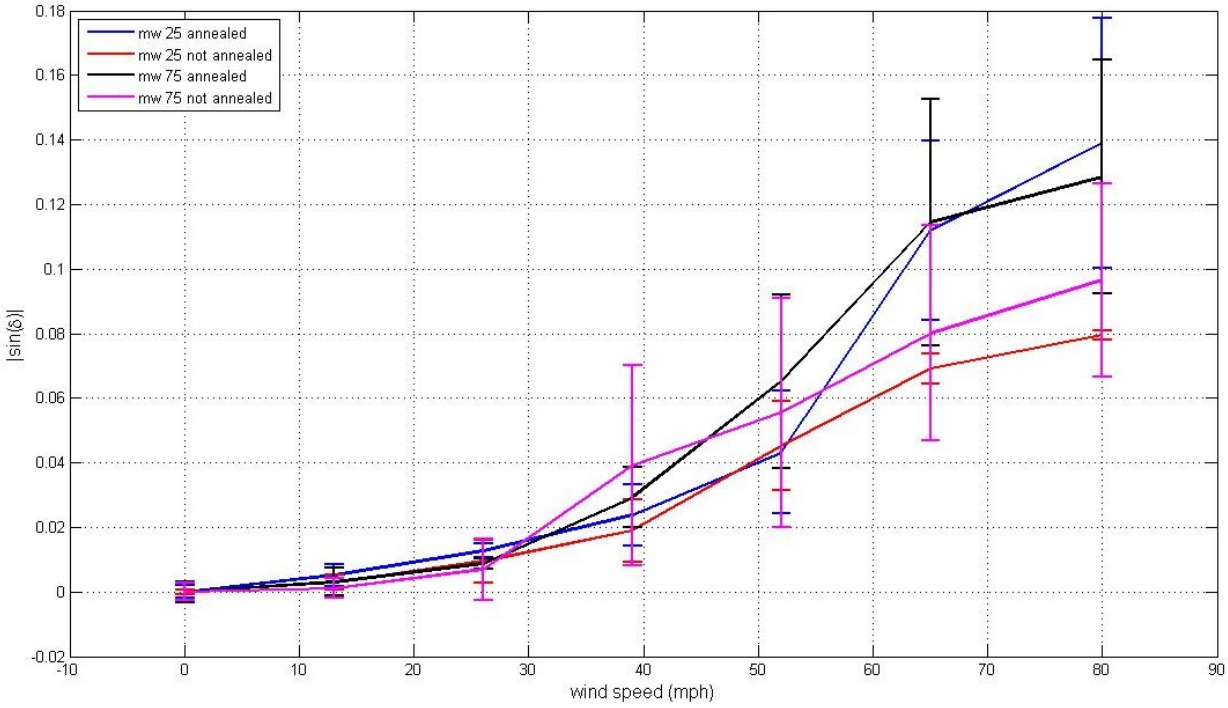

Figure 22: Wind Tunnel Annealing Effects.

Several interesting trends are apparent immediately. The first is that the benefit of annealing is clearly visible. For both molecular weights of PMMA, the peak birefringence is higher for the annealed slides than for the non-annealed ones. The other interesting trend is that there is little difference between the two molecular weights in terms of maximum birefringence. Note that in the case of the non-annealed samples, the higher molecular weight shows increased birefringence over the lower molecular weight. These results contradict the previous molecular weight study. This goes hand-in-hand with the third visible trend, which is the large error bars, particularly at the higher wind speeds. While the validity of these tests is questionable due to the contradictory results, it is clear that annealing does have some benefit.

In the calibration setup, three different scenarios were tested to cover the two variables: PDLC coating thickness and dry time. The slides were air-brushed and then dried at 30°C for one or two hours before being annealed at 80°C for one hour. The coating thickness was varied to cover thick and thin coatings based on the number of airbrush passes. Figure 23 shows the

results. According to the data, neither PDLC coating thickness nor dry time had a significant effect on birefringence. For the sake of expediency, the one hour dry method was adopted. Furthermore, to better ensure slide uniformity, thicker coatings were used for later testing.

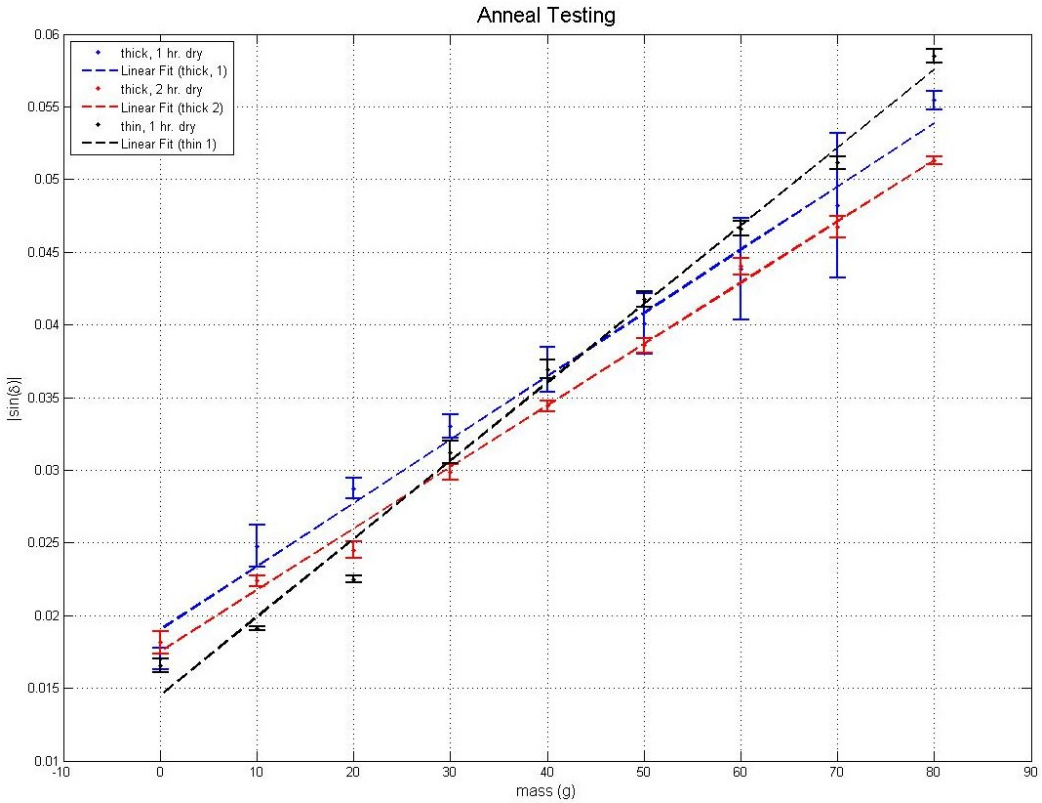

Figure 23: Comparative study of annealing parameters.

3.3 Sample Degradation

A simple test was done in the reflective mode calibration setup to determine the rate at which the samples degrade. To assess this, the same slide was tested a total of five times. The tests were spaced out over three days. Each test took three data points, and the standard deviation over the data was calculated. Figure 24 shows the results of tests 1, 4, and 5. As can clearly be seen, there is significant degradation between the various tests, with the peak birefringence value dropping from roughly 0.0475 to 0.0375 in the course of 5 tests, representing a loss of almost 25%.

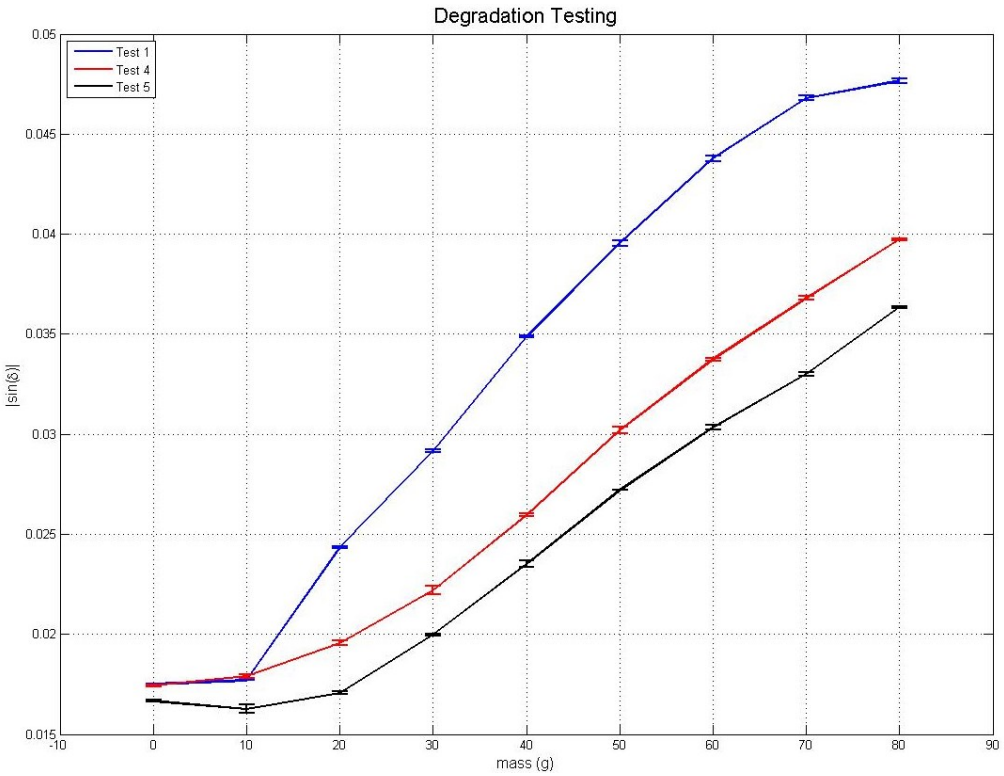

Figure 24: Effect of repeated tests on birefringence.

While sample degradation is an issue for wind tunnel applications, the issue was more severe in the case of the calibration setup. This is due to the nature of the shear force in the calibration setup itself being more severe. The action of the glass slides pulling against the polymer may have induced a failure mode within the polymer, resulting in the decrease in peak birefringence after multiple tests. As was previously mentioned, during the calibration setup tests the mass was not returned to zero between each test point, unlike in the wind tunnel where the wind was turned off and the slide allowed to drop back to zero birefringence between each test point. This is because, had the weights been removed, the slide would not have showed zero birefringence, indicating that some permanent failure had occurred. In general applications, it is presumed that each PDLC will be used for only one or two tests. Furthermore, this method is intended for wind tunnel applications, not manual shearing via weights, which results in a different shearing mechanism.

3.4 Reflective Backgrounds

A number of different reflective background materials were selected, but only the most promising were tested. To determine which were most promising, a simple pixel intensity check was performed using screenshots from MilliView and Matlab. Only the green color plane of the color CCD was checked, as the current MilliView system is best-calibrated for the green color plane. The full list of all materials considered can be found in Appendix A.

The results of the background tests done in the reflective mode calibration setup are shown in Figure 25. A total of five backgrounds were tested: Mylar, black, and three silvers. The Mylar was a strip cut from an emergency blanket. The black was a piece of paper spray painted black. The three silvers were silver spray paints: Krylon Silver, Krylon Chrome, and Design Master (DM) Silver. Two to three slides were tested for each background, with the error bars being representative of the standard deviation between all of the test points for each sample.

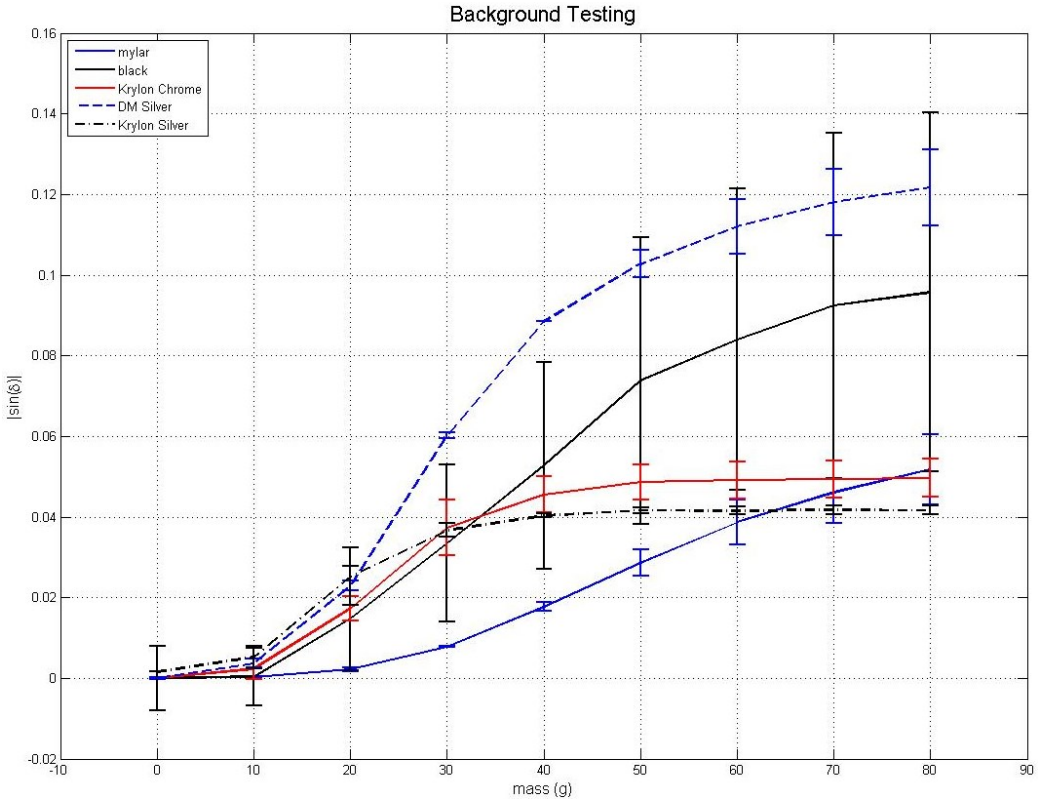

Figure 25: Comparison of reflective materials to be used as background.

Several interesting trends appeared. While the DM Silver and black backgrounds appeared to give the largest birefringence values, they also gave the largest errors. Furthermore, the DM Silver spray appeared to have partially melted as a result of the annealing process, which was used with the calibration setup slide sandwiches to make a more uniform layer between the two slides. While the Mylar background gave more linear birefringence results, it was decided that Mylar could not feasibly be used in future testing applications, since very few polymers would stick to Mylar. The final decision was then to consider either the Krylon Chrome or Krylon Silver spray for future testing. As the Krylon Silver gave slightly higher maximum birefringence values, it was chosen as the reflective background to be used in eventual reflective mode wind tunnel testing.

3.5 Reflective Mode

One of the major objectives of this research was to use the wind tunnel setup in reflective mode. Careful consideration was made to achieve sufficient lighting of the test samples. To ensure that no change in slide manufacturing techniques had occurred, wind tunnel testing in transmission mode was performed first before switching the configuration to reflective mode with the same LED lamp used in both tests. To further ensure that no degradation had occurred during the testing, fresh slides were prepared for each test. The slides were allowed to setup overnight to ensure that the polymer had fully cured. The PDLC coating was applied to the clear glass slides. A slide coated with Krylon silver spray paint was placed behind the coated slide to enable reflection.

Figure 26 shows the results of the transmission test (left) and reflection test (right). The transmission test results are similar to those pictured in Figure 18, the biggest difference being a decrease in peak birefringence values. Comparison to the reflective test results show a severe decrease in birefringence. This may be the result of a loss of light caused by the imperfect reflection of the silver spray paint. A highly polished aluminum surface might afford better reflective properties, but care would need to be taken to ensure that the surface was very smooth. However, while the loss in peak birefringence is still of concern, the overall trend of increasing birefringence with increasing wind speed coupled with a nominal return to zero implies that reflective PDLCs are viable shear sensors.

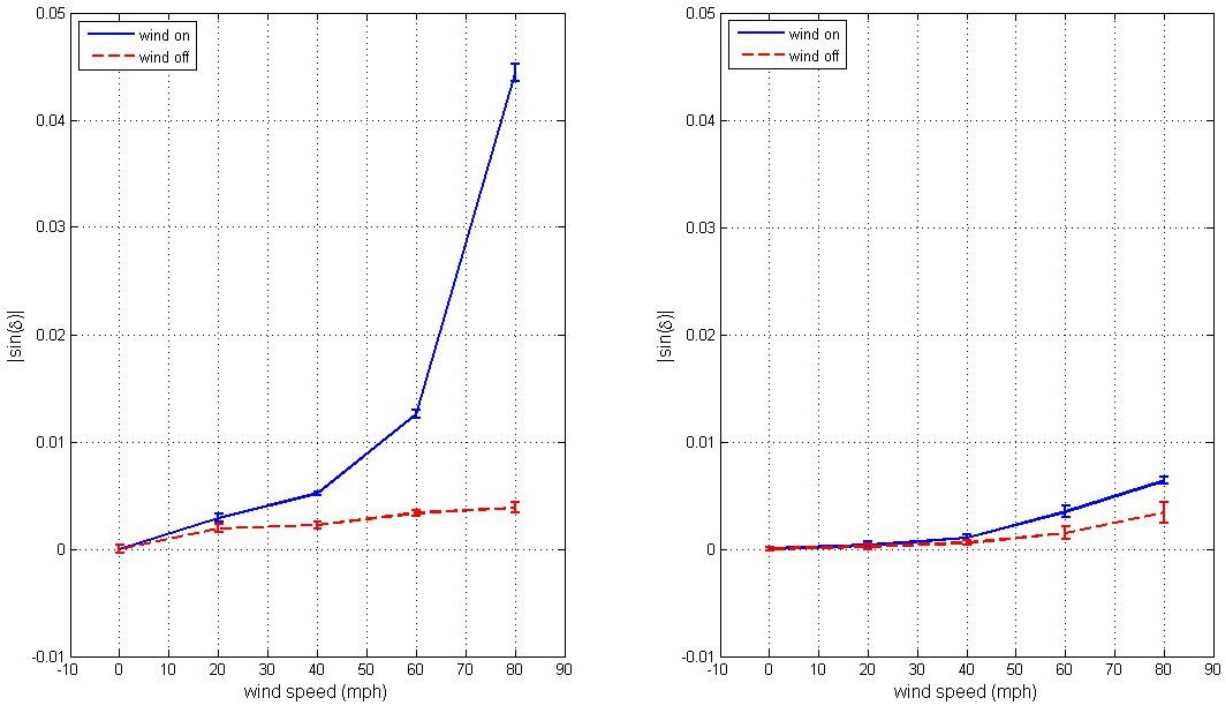

Figure 26: Comparison of wind tunnel transmissive vs. reflective modes.

3.6 Wedge Testing

The aluminum wedge, with its pointed front edge, allowed the flow to split slowly, resulting in a laminar boundary layer. The wedge was first sprayed with the Krylon silver spray to create a smooth, uniform reflective surface before receiving the layer of PDLC coating. The wedge was marked in 1cm segments, and the birefringence was measured at two stations for wind speeds up to 80mph in 16mph increments. To confirm that the boundary layer was indeed laminar, the Reynolds number was calculated for all speeds at both stations. The Reynolds number never went above $5x10^5$, the critical Reynolds number for a flat plate [29], meaning that the flow remained laminar at both stations for all speeds. A calibration curve based on Equation 13 and the laminar flow model presented in Equation 17.b was applied to the birefringence values calculated at both stations. The data are shown in Figure 27.

Based on Equation 17.b, the shear force is expected to decrease with increasing distance from the leading edge. This can be seen in the wedge test results. Higher peak birefringence values were observed at the station closer to the leading edge. The calibration curves resulted in R-squared values of 0.9258 and 0.7789 for the closer and farther stations, respectively.

Improvements in agreement could come from repeated testing, as the values for this test were taken as single time values instead of the time-average of three data points. This was due to the necessity to acquire data for multiple locations simultaneously. To guarantee that the same location was measured at each speed point, images were collected during the test and then analyzed afterwards as opposed to taking real-time measurements. As only one image was taken per speed point, an average was not available. Error bars are estimated based on typical test values.

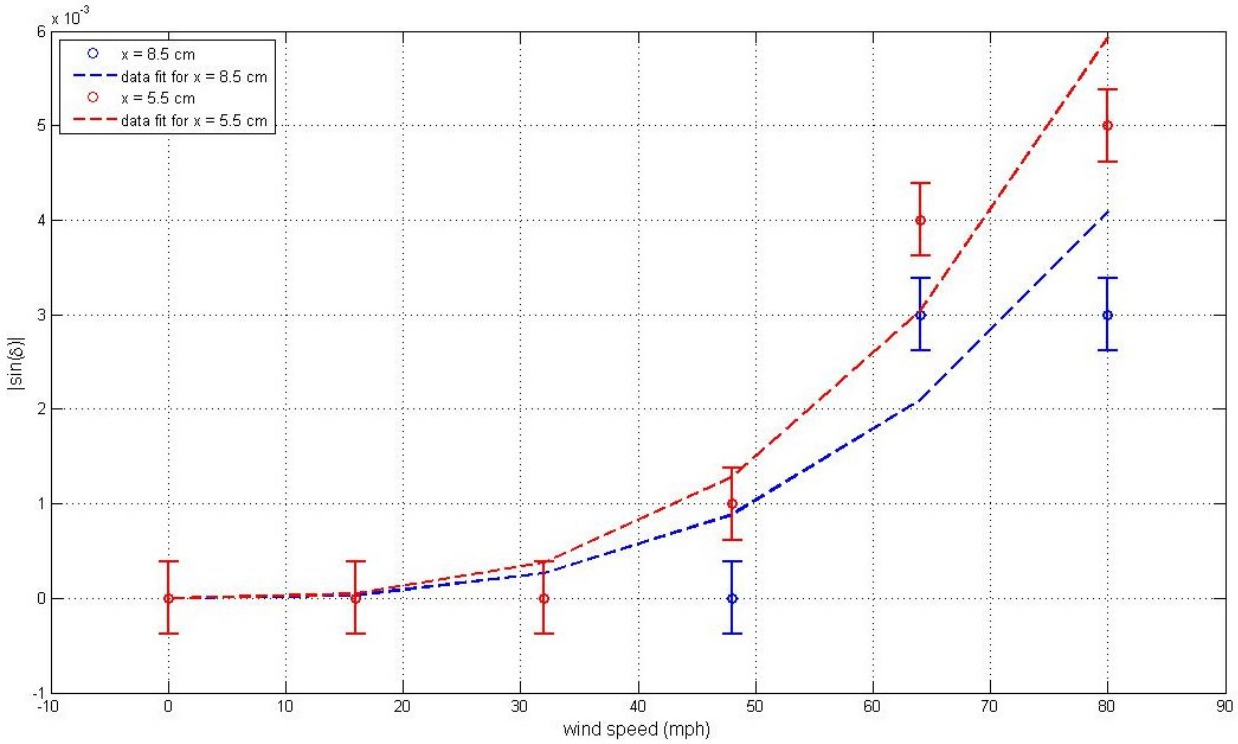

Figure 27: Results from aluminum wedge testing.

Chapter 4. Future Work

4.1 Enhanced Illumination

To improve signal strength in the reflective mode, two options exist: improvement in reflective surfaces, or improvement in lighting. The benefit of the currently used silver spray paint is the simplicity of use and availability. To find a suitable replacement that is comparable in those two aspects would be difficult. However, there are many possibilities in lighting improvements. One is the use of a powerful halogen lamp, focused through a lens. However, the ultraviolet radiation produced by a focused halogen lamp beam is strong enough to melt the plastic polarizer currently used. The procurement of a glass polarizer or a water filter would alleviate these issues.

Another possibility is the use of a green light source, or even a green laser. As seen in Equation 2, the phase shift is impacted by the wavelength of light. A laser would offer a more uniform wavelength, and could improve the amount of light seen by the camera as non-green light would not have to be discarded.

4.2 Production Methods Study

A number of production methods have been presented in this paper. However, only the SIPS and TIPS methods have been used. Specifically, the TIPS method was only used in the calibration setup and not in the wind tunnel setup. Exploration of a combined SIPS-TIPS method should be compared with the PIPS method of production in terms of sample quality. A further study should be done regarding LC-to-polymer ratio. While this paper focused on a 1:2 ratio, the optimal ratio may be something else.

4.3 Curved Surfaces

All airfoils have some curvature to them, and many of the NACA-designed airfoils exhibit some camber [29]. As a result any shear sensor designed to be used for aerodynamic research purposes must be able to measure the shear stress vectors along a curved surface. While

the curvature should not affect the birefringence of the liquid crystals, curved surfaces do provide difficulties with lighting. Uniform lighting of the sample is critical, especially in the case of reflective mode where not all of the light is being returned to the camera. A more powerful light source, such as a flood lamp, or multiple lights may be needed to compensate for curvature-induced dark areas. Direct comparison with a known airfoil would not only validate the PDLC method but would provide a more precise calibration curve between PDLC birefringence readings and tabulated shear force data.

4.4 Combination with Pressure-Sensitive Paint

The end goal of this research is to produce a paint that combines both pressure and shear-sensing attributes. The combination of these two would result in a highly efficient method for determining the aerodynamic forces on a body. Pressure-sensitive paint, or PSP, has already been developed and tested by Khalil et al [31], [32]. The ideal polymer for the PSP was determined to be the FIB polymer, a random co-polymer of heptafluoro-n-butyl methacrylate and hexafluoroisopropyl methacrylate developed at the University of Washington. The FIB polymer has previously been shown to be a valid polymer for use in PDLC sensors [33]. However, in combination with pressure-sensitive luminophors, the ratios of luminophor-to-polymer-to-solvent and liquid crystal-to-polymer-to-solvent may need to be adjusted to ensure optimization of both.

Another difficulty is the reflective surface. PSP often uses Titanium oxide plates, which are diffuse reflectors. However, diffuse reflectors were shown to produce zero birefringence readings. Therefore, a different reflective background would need to be chosen for the combined PSP-PDLC sensor.

Chapter 5. Conclusion

The appeal of a non-intrusive, simple-to-use shear sensor that gives truly 2-dimensional mapping is high. PDLCs represent one such method. Previous testing focused on the feasibility of a PDLC sensor in transmission mode, examining small areas. It was necessary, for expansion into practical applications, to show the feasibility of such a sensor in reflective mode and in larger areas. By utilizing shear forces created by a pulley-weight system as well as turbulent and laminar boundary layers, it has been demonstrated that the birefringence of polymer-dispersed liquid crystals still behaves as a shear sensor in reflection over larger areas. Additional attributes of the PDLC sensor were studies, such as the impact of annealing and the presence of degradation. While these results were obtained for the calibration setup only, they at least provide insight into possible improvements and issues in wind tunnel testing. It is clear that additional research is needed to make a PDLC shear measurement system commercially viable, but current progress indicates that it is not only feasible, but highly promising over the multitude of single point measurement systems. Furthermore, the inclusion of PSP within a PDLC sensor would revolutionize aerodynamics testing as the first truly all-inclusive, 2-dimensional aerodynamics forces measurement system.

References

[1] D. P. Raymer, "Sizing from a Conceptual Sketch," in *Aircraft Design*, 4th ed., Reston, Virginia: American Institute of Aeronautics and Astronautics, Inc., 2006, pp. 15-36.

[2] NASA Spinoff, "Winglets Save Billions of Dollars in Fuel Consumption," 2010. [Online]. Available: http://spinoff.nasa.gov/Spinoff2010/t_5.html. [Accessed 31 May 2014].

[3] C. Tropea, A. L. Yarin and J. F. Foss, "Wall-Bounded Flows," in *Springer Handbook of Experimental Fluid Mechanics*, Berlin, Springer, 2007, pp. 871-907.

[4] J. W. Naughton and M. Sheplak, "Modern developments in shear-stress measurement," *Progress in Aerospace Sciences,* vol. 38, pp. 515-570, 2002.

[5] L. C. Squire, "The motion of a thin oil sheet under the steady boundary layer on a body," *Journal of Fluid Mechanics,* vol. 11, no. 02, pp. 161-179, 1961.

[6] L. H. Tanner and L. G. Blows, "A study of the motion of oil films on surfaces in air flow, with application to the measurement of skin friction," *Journal of Physcics E: Scientific Instruments,* vol. 9, no. 3, pp. 194-202, 1976.

[7] F. Jiang, Y.-C. Tai, B. Gupta, R. Goodman, S. Tung, J.-B. Huang and C.-M. Ho, "A Surface Micro-Machined Shear Stress Imager," in *Micro Electro Mechanical Systems*, San Diego, 1996.

[8] M. Hites, H. Nagib and C. Wark, "Velocity and wall shear-stress measurements in high-Reynolds-number turbulent boundary layers," in *28th Fluid Dynamics Conference*, 1997.

[9] I.-C. Khoo, "Introduction to Liquid Crystals," in *Liquid Crystals*, 2nd ed., Hoboken, New Jersey: John Wiley & Sons, Inc., 2007, pp. 1-21.

[10] D. C. Reda and M. C. Wilder, "Shear-Sensitive Liquid Crystal Coating Method Applied Through Transparent Test Surfaces," *AIAA Journal,* vol. 39, no. 1, pp. 195-197, 2001.

[11] D. C. Reda, M. C. Wilder, D. J. Farina and G. Zilliac, "New Methodology for the Measurement of Surface Shear Stress Vector Distributions," *AIAA Journal,* vol. 35, no. 4, pp. 608-614, 1997.

[12] D. C. Reda, M. C. Wilder, R. D. Mehta and G. Zilliac, "Measurement of Continuous Pressure and Shear Distributions Using Coating and Imaging Techniques," *AIAA Journal,* vol. 36, no. 6, pp. 895-899, 1998.

[13] N. Fujisawa, Y. Oguma and T. Nakano, "Measurements of wall-shear-stress distribution on an NACA0018 airfoil by liquid-crystal coating and near-wall particle imaging velocimetry (PIV)," *Measurement Science and Technology,* vol. 20, pp. 1-10, 2009.

[14] D. R. Buttsworth, S. J. Elston and T. V. Jones, "Skin friction measurements on reflective surfaces using nematic liquid crystal," *Experiments in Fluids,* vol. 28, pp. 64-73, 2000.

[15] A. M. Glazer, J. G. Lewis and W. Kaminsky, "An Automatic Optical Imaging System for

Birefringent Media," *Proceedings: Mathematical, Physical and Engineering Sciences,* vol. 452, no. 1995, pp. 2751-2765, 1996.

[16] C. A. McFarland, J. L. Koenig and J. L. West, "Analysis of Polymer-Dispersed Liquid Crystals by Infrared Spectroscopy," *Applied Spectroscopy,* vol. 47, no. 3, pp. 321-329, 1993.

[17] M. Mucha, "Polymer as an important component of blends and composites with liquid crystals," *Progress in Polymer Science,* vol. 28, pp. 837-873, 2003.

[18] D. S. Parmar and J. J. Singh, "Partially exposed polymer dispersed liquid crystals for boundary layer investigations," *Appl. Phys. Lett.,* vol. 61, no. 17, pp. 2039-2041, 1992.

[19] C. A. McFarland, J. A. Koenig and J. L. West, "Influence of the Polymer Matrix on the Bipolar and Radial Droplet Configurations within PDLC Films Examined by Infrared Spectroscopy," *Journal of Applied Spectroscopy,* vol. 47, no. 5, pp. 598-605, 1993.

[20] I. G. Wood and A. M. Glazer, "Ferroelastic Phase Transition in BiVO4. I. Birefringence Measurements Using the Rotating-Analyser Method.," *Journal of Applied Crystallography,* vol. 13, pp. 217-223, 1980.

[21] Wikipedia, "Polarizer," 1 April 2010. [Online]. Available: http://en.wikipedia.org/wiki/Polarizer#mediaviewer/File:Circular.Polarizatio%20n.Circularly.Polarized.Light_Circular.Polarizer_Passing.Left.Handed.Helix.Vi%20ew.svg.. [Accessed 22 June 2014].

[22] E. M. Spiesz, W. Kaminsky and P. K. Zysset, "A quantitative collagen fibers orientation assessment using birefringence measurements: Calibration and application to human osteons," *Journal of Structural Biography,* vol. 176, pp. 302-306, 2011.

[23] W. Kaminsky, E. Gunn, R. Sours and B. Kahr, "Simultaneous false-colour imaging of birefringence, extinction and transmittance at camera-speed," *Journal of Microscopy,* vol. 228, no. 2, pp. 153-164, 2007.

[24] S.-T. Wu and D.-K. Yang, "Liquid Crystal/Polymer Composites," in *Reflective Liquid Crystal Displays*, Chichester, West Sussex: John Wiley & Sons, Ltd., 2001, pp. 149-195.

[25] P. Formentin, R. Palacios, J. Ferre-Borrull, J. Pallares and L. F. Marsal, "Polymer-dispersed liquid crystal based on E7: Morphology and characterization," *Synthetic Metals,* vol. 158, pp. 1004-1008, 2008.

[26] J. L. West, "Phase Separation of Liquid Crystals in Polymers," *Mol. Cryst. Liq. Cryst. Inc. Nonlin. Opt.,* vol. 157, pp. 427-441, 1988.

[27] R. G. Budynas, "Force, Stress, Strain, and Displacement," in *Advanced Strength and Applied Stress Analysis*, 2nd ed., McGraw-Hill, 1999, pp. 23-24.

[28] J. D. Anderson, "Basic Aerodynamics," in *Introduction to Flight*, 6th ed., New York, McGraw-Hill, 2008, pp. 210-215.

[29] J. D. Anderson, "Incompressible Flow over Airfoils," in *Fundamentals of Aerodynamics*,

5th ed., New York, New York: McGraw-Hill, 2011, pp. 313-409.

[30] F. M. Kimura, *Novel Measurement Techniques for the Study of Unsteady Flow Phenomena: Shear Sensitive Paint and Present Sensitive Microspheres,* Ann Arbor: Proquest, 2009.

[31] G. E. Khalil, C. Costin, J. Crafton, G. Jones, S. Grenoble, M. Gouterman, J. B. Callis and L. R. Dalton, "Dual-luminophor pressure-sensitive paint: I. Ratio of reference to sensor giving a small temperature dependency," *Sensors and Actuators B,* vol. 97, pp. 13-21, 2004.

[32] M. Gouterman, J. Callis, L. Dalton, G. Khalil, Y. Mebarki, K. R. Cooper and M. Grenier, "Dual luminophor pressure-sensitive paint: III. Application to automotive model testing," *Measurement Science and Technology,* vol. 15, pp. 1986-1994, 2004.

[33] G.-S. Li, K. Low, L. Chen, F. Kimura, J. B. Callis, W. Kaminsky, G. E. Khalil and D. Dabiri, "High Resolution Shear Stress Measurements from Imaging Polarimetry," in *Int. Symp on Appl. Laser Techniques to Fluid Mechanics*, Lisbon, 2012.

[34] W. Kaminsky, "Real-time Linear-birefringence-detecting Polarization Microscope". United States of America Patent 7,522,278 B2, 21 April 2009.

Appendix A

Table 1 below lists all of the reflective materials tested for the background test. Pixel values for the green light were measured directly using Matlab. The values were then compared with aluminum.

Table 1: List of all reflective materials tested.

Material	pixel value	percent increase in reflectivity
Reflect-All on silver	83.7	-11
Krylon silver spray paint	85.1	-10
aluminum	94.5	0
reflective tape	95.3	1
aluminum foil	97.2	3
Reflect-All on white	120	27
white paper	123.5	31
Mylar	127.6	35
mirror	132.4	40
Ti-Oxide plate	135	43

Appendix B

The full derivation of the birefringence measurement method is taken from [34]. This section covers the steps taken to achieve Equation 8 given Equations 5 and 6. To begin, the angles $0, \frac{\pi}{4}, \frac{\pi}{2}, \frac{3\pi}{4}$, corresponding to 0, 45, 90, and 135, are plugged into Equation 5, resulting in four intensity values. The least-squares method is then used the minimize the function below

$$D = \sum_{i=1}^{4} \frac{1}{w}(I_i - I_c)^2 \tag{B1}$$

where I_i corresponds to an intensity measured at each angle, I_c corresponds to the four intensity values found from Equation 5 by plugging in the angles, and w is a weighting factor that will be ignored in the following derivation. To minimize D requires minimizing the partial differentials with respect to each coefficient, namely

$$\frac{\partial D}{\partial a_0} = 0, \qquad \frac{\partial D}{\partial a_1} = 0, \qquad \frac{\partial D}{\partial a_2} = 0 \tag{B2}$$

The three partial differential equations then become

$$\frac{\partial D}{\partial a_0} = \sum_{i=1}^{4} 2(I_i - I_c) \tag{B3.a}$$

$$\frac{\partial D}{\partial a_1} = \sum_{i=1}^{4} 2(I_i - I_c)x_{1i} \tag{B3.b}$$

$$\frac{\partial D}{\partial a_2} = \sum_{i=1}^{4} 2(I_i - I_c)x_{2i} \tag{B3.c}$$

where $x_{1i} = \sin(2\alpha_i)$ and $x_{2i} = \cos(2\alpha_i)$. Once again using Equation 5, these can be represented in matrix form as below

$$\begin{bmatrix} \sum_{i=1}^{4} I_i \\ \sum_{i=1}^{4} I_i x_{1i} \\ \sum_{i=1}^{4} I_i x_{2i} \end{bmatrix} = \begin{bmatrix} \sum_{i=1}^{4} 1 & \sum_{i=1}^{4} x_{1i} & \sum_{i=1}^{4} x_{2i} \\ \sum_{i=1}^{4} x_{1i} & \sum_{i=1}^{4} x_{1i}^2 & \sum_{i=1}^{4} x_{1i}x_{2i} \\ \sum_{i=1}^{4} x_{2i} & \sum_{i=1}^{4} x_{1i}x_{2i} & \sum_{i=1}^{4} x_{2i}^2 \end{bmatrix} \begin{bmatrix} a_0 \\ a_1 \\ a_2 \end{bmatrix} \tag{B4}$$

Table 2 summarizes the values taken by x_{1i} and x_{2i} at the different angles.

Table 2: Values used in matrix equations.

Angle α_i	$x_{1i} = \sin(2\alpha_i)$	$x_{2i} = \cos(2\alpha_i)$
0	0	1
π/4	1	0
π/2	0	-1
3π/4	-1	0

Plugging these values into matrix B4 results in the following simplifications

$$\begin{bmatrix} I_1 + I_2 + I_3 + I_4 \\ I_2 - I_4 \\ I_1 - I_3 \end{bmatrix} = \begin{bmatrix} 4 & 0 & 0 \\ 0 & 2 & 0 \\ 0 & 0 & 2 \end{bmatrix} \begin{bmatrix} a_0 \\ a_1 \\ a_2 \end{bmatrix} \tag{B5}$$

The diagonal matrix is invertible, and the coefficients can be easily solved for by left-multiplying the intensity matrix, as seen below.

$$\begin{bmatrix} \frac{1}{4} & 0 & 0 \\ 0 & \frac{1}{2} & 0 \\ 0 & 0 & \frac{1}{2} \end{bmatrix} \begin{bmatrix} I_1 + I_2 + I_3 + I_4 \\ I_2 - I_4 \\ I_1 - I_3 \end{bmatrix} = \begin{bmatrix} a_0 \\ a_1 \\ a_2 \end{bmatrix} \tag{B6}$$

This results in the following solutions for the three coefficients

$$a_0 = \frac{1}{4}(I_1 + I_2 + I_3 + I_4), \quad a_1 = \frac{1}{2}(I_2 - I_4), \quad a_2 = \frac{1}{2}(I_1 - I_3) \tag{B7}$$

Calculations are done on a pixel-by-pixel basis, with the birefringence and extinction angle given in Equations 9 and 10, and the transmittance given simply by a_0.